The Astrophysical Journal, 877:18 (22pp), 2019 May 20 https://doi.org/10.3847/1538-4357/ab18f8

Radial Acceleration Relation between Baryons and Dark or Phantom Matter in the Supercritical Acceleration Regime of Nearly Spherical Galaxies

Kyu-Hyun Chae[1,2], Mariangela Bernardi[3], Ravi K. Sheth[3], and In-Taek Gong[2]
[1] Department of Physics and Astronomy, Sejong University, 209 Neungdong-ro Gwangjin-gu, Seoul 05006, Republic of Korea; chae@sejong.ac.kr, kyuhyunchae@gmail.com
[2] Graduate Program of Astronomy and Space Science, Sejong University, 209 Neungdong-ro Gwangjin-gu, Seoul 05006, Republic of Korea
[3] Department of Physics and Astronomy, University of Pennsylvania, 209 South 33rd Street, Philadelphia, PA 19104, USA; bernardm@physics.upenn.edu, shethrk@physics.upenn.edu
Received 2018 November 27; revised 2019 April 8; accepted 2019 April 11; published 2019 May 17

Abstract

The central regions of nearby elliptical galaxies are dominated by baryons (stars) and provide interesting laboratories for studying the radial acceleration relation (RAR). We carry out exploratory analyses and discuss the possibility of constraining the RAR in the supercritical acceleration range $(10^{-9.5}, 10^{-8})\ \mathrm{m\,s^{-2}}$ by using a sample of nearly round pure-bulge (spheroidal, dispersion-dominated) galaxies. This sample includes 24 ATLAS^{3D} galaxies and 4201 SDSS galaxies, and covers a wide range of masses, sizes, and luminosity density profiles. We consider a range of current possibilities for the stellar mass-to-light ratio ($M_\star/L$), its gradient, and dark or phantom matter (DM/PM) halo profiles. We obtain the probability density functions (PDFs) of the parameters of the considered models via Bayesian inference based on spherical Jeans Monte Carlo modeling of the observed velocity dispersions. We then constrain the DM/PM-to-baryon acceleration ratio a_X/a_B from the PDFs. Unless we ignore observed radial gradients in $M_\star/L$, or assume unreasonably strong gradients, marginalization over nuisance factors suggests $a_X/a_B = 10^p(a_B/a_{+1})^q$ with $p = -1.00 \pm 0.03$ (stat) $^{+0.11}_{-0.06}$ (sys) and $q = -1.02 \pm 0.09$ (stat) $^{+0.16}_{-0.00}$ (sys) around a supercritical acceleration $a_{+1} \equiv 1.2 \times 10^{-9}\ \mathrm{m\,s^{-2}}$. In the context of the ΛCDM paradigm, this RAR suggests that the NFW DM halo profile is a reasonable description of galactic halos even after the processes of galaxy formation and evolution. In the context of the MOND paradigm, this RAR favors the "Simple" interpolating function but is inconsistent with the vast majority of other theoretical proposals and fitting functions motivated mainly by subcritical acceleration data.

Key words: dark matter – galaxies: kinematics and dynamics – galaxies: structure – gravitation

1. Introduction

Mass discrepancy in galaxies—the disagreement between the mass inferred from the observed light distribution and that derived from kinematics of stars and gases or gravitational lensing under the standard Newton–Einstein gravity and dynamics—remains an unsolved problem for fundamental physics and cosmology. Proposed resolutions of the mystery broadly fall into two classes: either much of the gravitating mass is dark matter (DM), or our current understanding of gravity or dynamics must be modified (MG) (e.g., Famaey & McGaugh 2012; Bertone & Tait 2018).

Recent decades have witnessed the surprising observation that the mass discrepancy becomes prominent only when the (centripetal) radial acceleration is weaker than a critical value $a_0 \sim 10^{-10}\ \mathrm{m\,s^{-2}}$. In this regime, the observed radial acceleration traced by the circular velocity V, $a = V^2/r$, correlates well with the Newtonian radial acceleration predicted by the distribution of baryons, a_B (e.g., McGaugh 2004; McGaugh et al. 2016; Lelli et al. 2017). The radial acceleration relation (RAR), or mass discrepancy–acceleration relation, is now well-documented for rotating galaxies, particularly in the low (subcritical) acceleration regime $a_B < 10^{-10}\ \mathrm{m\,s^{-2}}$ (McGaugh et al. 2016; Lelli et al. 2017; Li et al. 2018).

The empirical RAR has recently prompted hydrodynamic-simulation (e.g., Keller & Wadsley 2017; Ludlow et al. 2017; Tenneti et al. 2018) and semi-analytic (e.g., Desmond 2017; Navarro et al. 2017) studies in the standard Lambda cold dark matter (ΛCDM) paradigm. In the ΛCDM paradigm, the empirical RAR simply represents an average property of galaxies that is a consequence of galactic astrophysics: as such, there is no need for all galaxies to follow the same RAR. However, it is argued that ΛCDM has difficulty in reproducing (van Putten 2018), or can only qualitatively reproduce (Lelli et al. 2017; Tenneti et al. 2018), the empirical RAR. Whether the empirical RAR arises naturally in the ΛCDM paradigm and whether its approximate universality indicates a deeper Kepler-like law of galactic dynamics (see Kroupa et al. 2018; McGaugh et al. 2018; Rodrigues et al. 2018) are currently open questions.

For spherical gravitating systems, the empirical RAR $a = a(a_B)$ [or $a_B = a_B(a)$] can be written as

$$a(r) = G\frac{M_B(r) + M_{DM}(r)}{r^2} = \left(1 + \frac{a_{DM}(r)}{a_B(r)}\right)a_B(r) \quad (1)$$

assuming DM, or

$$a(r) = f\left(\frac{a_B(r)}{a_0}\right)a_B(r) \quad (2)$$

assuming modified Newtonian dynamics (MOND) (Milgrom 1983) or MG. In Equation (1), G is Newton's gravitational constant and $M_i(r)$ is the mass within the spherical radius r for the ith component. In Equation (2), $f(x)$ is a fitting function known as the interpolating function (IF). These approaches can be parameterized in a unified way by introducing "phantom"

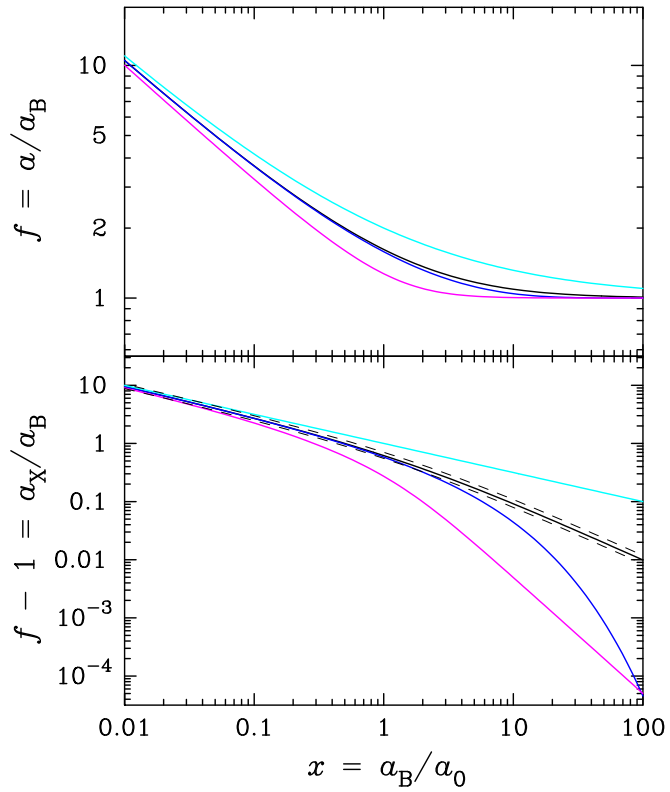

Figure 1. Various fitting (interpolating) functions of the RAR in the form of $f = a/a_B$ (top) or $f - 1 = a_X/a_B$. The colors in each panel signify the following: black is used for the Simple IF (Equation (4), $\nu = 1$), magenta for the Standard IF (Equation (4), $\nu = 2$), blue signifies McGaugh's IF (Equation (5), $\lambda = 1$), and cyan is used for Bekenstein's IF (Equation (6), $\gamma = 1/2$). The thin black dashed curves in the bottom panel indicate the effects of varying a_0 from a fiducial value of 1.2 (e.g., in units of 10^{-10} m s^{-2}) to 1.0 and 1.4, respectively.

matter (PM) into MG as follows:

$$\frac{a}{a_B} - 1 = f\left(\frac{a_B}{a_0}\right) - 1 \equiv \frac{a_X}{a_B}, \tag{3}$$

where X denotes DM or PM. Working with a_X hides the fact that, in ΛCDM, one treats the discrepancy between what the light predicts and what is observed by adding an independent term, $M_{DM}(r)$ to the total mass. In MOND, the amount to be "added" depends on what is present.

Several functional forms (see Figure 1), either empirically motivated or inspired by theory, have been suggested for the RAR. These include the "Simple" function (Famaey & Binney 2005), the "Standard" function (Kent 1987), McGaugh's function (McGaugh 2008), and Bekenstein's function (Bekenstein 2004). Among the theoretical proposals are Bekenstein's modified gravity (Bekenstein 2004), Verlinde's emergent gravity (Verlinde 2017), a symmetron-like fifth force (Burrage et al. 2017), and modified properties of DM such as superfluidity (Berezhiani & Khoury 2015) or dipolarity (Blanchet & Le Tiec 2009).

We will consider three families of models under the MOND paradigm. First,

$$f_\nu(x) = \left(\frac{1}{2} + \sqrt{\frac{1}{4} + \frac{1}{x^\nu}}\right)^{1/\nu}, \tag{4}$$

with $0 < \nu \leqslant 2$; this includes the Simple ($\nu = 1$) and Standard ($\nu = 2$) IFs as special cases. Second,

$$f_\lambda(x) = \frac{1}{(1 - e^{-x^{\lambda/2}})^{1/\lambda}}, \tag{5}$$

with $0.3 < \lambda < 1.7$, which includes McGaugh's IF ($\lambda = 1$) as a special case. Third,

$$f_\gamma(x) = 1 + \frac{1}{x^\gamma}, \tag{6}$$

with $0 < \gamma < 2$, which includes Bekenstein's IF ($\gamma = 1/2$) as a special case.

In MOND, both the IF shape (the value of ν, λ or γ) and the scale a_0 are assumed to be the same for all galaxies. While there is general agreement that $a_0 \approx 1.2 \times 10^{-10}$ m s^{-2}, there is less agreement on the shape. Although several previous RAR studies favored the Simple IF (e.g., Famaey & Binney 2005; Sanders & Noordermeer 2007; Milgrom 2012; Chae & Gong 2015; Janz et al. 2016), a recent series of analyses (McGaugh et al. 2016; Lelli et al. 2017; Li et al. 2018) argue that all galaxies follow McGaugh's IF. This has far-reaching implications: any theory of DM or MG that does not predict the exponential decay of a_X/a_B in the high-acceleration limit would be ruled out. For example, a recent proposal of DM–baryon interactions (Famaey et al. 2018) would be invalidated by McGaugh's function.

However, the top panel of Figure 1 shows that, if one only considers the ratio a/a_B, which has been the focus of RAR studies to date, then there is only a subtle difference between McGaugh's IF and the Simple IF. On the other hand, as the bottom panel shows, the quantity a_X/a_B provides greater discriminatory power, especially in the supercritical ($a_0 > 1.2 \times 10^{-10}$ m s^{-2}) regime. (Note that changing a_0 merely shifts curves left or right; reasonable ∼20% changes in a_0 cannot bring one IF into agreement with another. This will simplify some of our analysis below.) Because the existence and form of the RAR has fundamental implications, this work is focused on the supercritical acceleration regime.

In this work, we use a Bayesian inference of the ratio a_X/a_B (Figure 1), based on Jeans dynamical analyses of nearly spherical galaxies. There are several reasons for using spherical galaxies. First, the optical regions within the effective radius R_e, which is defined as the two-dimensional radius (projected on the plane of the sky) containing one-half of the total light, cover the supercritical acceleration range 10^{-10} m s$^{-2} \lesssim a_B \lesssim 10^{-8}$ m s^{-2}. Second, they can be described by spherical models, avoiding the uncertainties related to angular dependences. Third, spherical galaxies are dispersion (pressure)-supported systems dynamically distinct from rotationally supported systems, and hence they provide an independent probe of the RAR. Indeed, there exists previous work arguing that the RAR for ellipticals differs from that for disk galaxies (e.g., Gerhard et al. 2001; Janz et al. 2016). Finally, spherical systems allow the most straightforward tests of theories. In particular, Verlinde's emergent gravity has a specific prediction only for spherical systems.

To constrain a_X/a_B in the supercritical regime using elliptical galaxies, a number of factors have to be dealt with carefully. In particular, radial gradients in the stellar mass-to-light ratio $\Upsilon_\star \equiv M_\star/L$ in the central regions of elliptical galaxies (e.g., Martín-Navarro et al. 2015; La Barbera et al. 2016; van Dokkum et al. 2017; Oldham & Auger 2018;

Sarzi et al. 2018; Sonnenfeld et al. 2018) can affect the inferred a_X/a_B (Bernardi et al. 2018). The effects of these gradients have been neglected in previous RAR analyses, so here we will pay particular attention to them, following the methodology of Chae et al. (2018).

We carry out our analyses in both the ΛCDM and MOND paradigms, because the empirical RAR has different implications for the two paradigms. In ΛCDM, a universal RAR is not required by theory; hence, by constraining RARs for individual galaxies and then averaging over the population, one obtains a mean RAR that may be useful for constraining the gastrophysics of galaxies. However, in the case of MOND, a single RAR is supposed to apply universally for *all* galaxies; ergo, the theory can be falsified if one can demonstrate that there are statistically significant variations across the population (e.g., from one elliptical galaxy to another) or between populations (e.g., ellipticals versus spirals).

This paper is structured as follows. In Section 2, we describe the data as well as the ΛCDM and MOND models we consider. In Section 3, we apply our Bayesian methodology to infer parameters in the ΛCDM paradigm. Specifically, we first describe our Monte Carlo (MC) sampling and Bayesian inference methods in Section 3.1, and then derive RARs of individual galaxies where dynamical information over a range of scales is available in Section 3.3. We discuss what these individual RARs imply for MOND in Section 3.4. In Section 3.5, we modify our methods to analyze galaxies where information from only a single scale is available. In Section 3.6, we derive an average, empirical RAR by stacking together all the individual results, and compare it with a number of MOND predictions. In Section 4, we provide a similar analysis, but now explicitly under the MOND paradigm. Section 4.3 discusses the issue of universality, and Section 4.4 provides direct χ^2 tests of MOND models using the observed velocity dispersion profiles of the most spherical galaxies. In Section 5, we discuss potential systematic errors and why we do not think they have biased our results. Finally, in Section 6, we discuss the implications of our exploratory results for DM or MG, as well as future prospects of using integral field spectroscopy (IFS) data on elliptical galaxies for the DM/MG problem. Appendix A discusses MC sampling methods and their effects on our Bayesian inferences. Appendix B presents examples of full parameter correlations from our modeling results of the four roundest galaxies in our sample. Throughout this paper, we use the following cosmological parameters whenever working in the ΛCDM framework: $\Omega_{m\,0} = 0.3$, $\Omega_{\Lambda 0} = 0.7$, and $h = H_0/100\,\mathrm{km\,s^{-1}\,Mpc^{-1}} = 0.7$.

2. Data and Method

2.1. Data Sets

We use nearly round pure-bulge (i.e., pure ellipsoids without detectable disks) galaxies selected from the ATLAS^{3D} project (Cappellari et al. 2011) and the SDSS DR7 (Abazajian et al. 2009); see Chae et al. (2018, 2019) for details of our sample selection. Of the 24 ATLAS^{3D} galaxies we select (from a total of 260), 16 are kinematic slow rotators (SRs). We require SDSS galaxies to be statistically similar to the ATLAS^{3D} galaxies, and so select 4201 galaxies from the UPenn spectroscopic catalog of about 0.7 million galaxies (Meert et al. 2015).

In these galaxies, individual stellar velocities and orbits are not observed, but the rms scatter of the line-of-sight velocity component, referred to as the velocity dispersion, is observed through Doppler broadening of spectral lines. However, ATLAS^{3D} provides more information about the velocity dispersion than does SDSS. Specifically, for each ATLAS^{3D} galaxy, a two-dimensional map of the line-of-sight velocity dispersions is available, from the central region out to (approximately) the projected half-light radius R_e. From these, we construct $\sigma_{los}(R)$, the line-of-sight velocity dispersion profile (Chae et al. 2018). (Throughout this paper, a capitalized R refers to a scale projected onto the plane of the sky.) We also have a measured surface brightness profile $I(R)$ out to a few R_e, which can be deprojected to give the volume density profile of luminosity $\rho_L(r)$ (we use the lower case r to indicate that it is a three-dimensional rather than projected quantity).

For SDSS galaxies, the line-of-sight velocity dispersion is only measured within a single aperture of radius $R_{ap} = D \times \theta_{ap}$, where $\theta_{ap} = 1.5$ arcsec and D is the angular-size distance to the galaxy. This quantity is related to the hidden profile by

$$\sigma_{ap} \equiv \langle \sigma_{los} \rangle (R_{ap}) = \frac{\int_0^R I(R')\,\sigma_{los}(R')\,R'dR'}{\int_0^R I(R')\,R'dR'}, \quad (7)$$

where $\sigma_{los}(R)$ is the velocity dispersion profile and $I(R)$ is the surface brightness distribution. Therefore, as we describe below, our treatment of SDSS galaxies will be slightly different than for ATLAS^{3D}.

2.2. Relation to the Jeans Equation

The line-of-sight velocity dispersion at projected radius R on the sky is related to the three-dimensional dispersion by

$$\sigma_{los}^2(R) = \frac{2}{I(R)} \int_R^\infty \rho_L(r)\,\sigma_r^2(r) \left[1 - \frac{R^2}{r^2}\beta(r)\right] \frac{r dr}{\sqrt{r^2 - R^2}}, \quad (8)$$

where $\sigma_r^2(r)$ is the radial velocity dispersion and $\beta(r) \equiv 1 - \sigma_t^2(r)/\sigma_r^2(r)$, where $\sigma_t^2(r) \equiv [\sigma_\theta^2(r) + \sigma_\phi^2(r)]/2$ is the velocity dispersion in the tangential (i.e., angular in the spherical polar coordinates) direction, is the velocity dispersion anisotropy.

In principle, the spherical Jeans equation (Equation (4.215) of Binney & Tremaine 2008)—which is satisfied if spherical galaxies are in equilibrium—allows the observed line-of-sight velocity dispersions to constrain the acceleration $a(r)$, where a is given by either Equation (1) (ΛCDM) or Equation (2) (MOND). This is because the spherical Jeans equation relates $\sigma_r^2(r)$ to $a(r)$:

$$\frac{d[\rho_B(r)\,\sigma_r^2(r)]}{dr} + 2\frac{\beta(r)}{r}[\rho_B(r)\,\sigma_r^2(r)] = -\rho_B(r)\,a(r), \quad (9)$$

where $\rho_B(r)$ is the density profile of the baryons. For our pure-bulge systems, we assume this is the same as that of the stellar mass, such that $\rho_B(r) \equiv \Upsilon_\star(r)\,\rho_L(r)$, where $\rho_L(r)$ is the deprojected light profile and $\Upsilon_\star \equiv M_\star/L$ is the stellar mass-to-light ratio. Note that $a(r) = a_B(r) + a_X(r)$, where a_B depends on the baryonic profile $\rho_B(r)$ whereas $a_X(r)$ depends on the DM or PM profile $\rho_X(r)$ (Equation (3)).

Table 1
Relation between Stellar Mass and Halo Mass in the ΛCDM Framework

$\log_{10}(M_\star^{\rm Krou}/M_\odot)$ (1)	$\log_{10}(M_{200}^{\rm WL}/M_\odot)$ (2)	Used Uncertainty (3)
10.39	$12.325^{+0.19}_{-0.24}$	$\sqrt{0.22^2+0.083^2}$
10.70	$12.295^{+0.12}_{-0.14}$	$\sqrt{0.13^2+0.083^2}$
10.97	$12.655^{+0.04}_{-0.05}$	$\sqrt{0.05^2+0.083^2}$
11.20	$13.045^{+0.04}_{-0.04}$	$\sqrt{0.04^2+0.083^2}$
11.38	$13.405^{+0.03}_{-0.03}$	$\sqrt{0.03^2+0.083^2}$
11.56	$13.785^{+0.03}_{-0.03}$	$\sqrt{0.03^2+0.083^2}$
11.75	$14.205^{+0.05}_{-0.05}$	$\sqrt{0.05^2+0.083^2}$

Note. (1) MPA-JHU stellar mass for the Kroupa IMF. (2) Estimated weak-lensing mass within a sphere of r_{200} from Mandelbaum et al. (2016). (3) Uncertainties that were actually used: the additional factor of 0.083 is included to account for the uncertainty associated with $M_\star^{\rm Krou}$. For $\log_{10}(M_\star^{\rm Krou}/M_\odot) \gtrsim 11$, these values are a factor of 2 smaller than what were shown in Figure 1 of Chae et al. (2018). These choices of uncertainties do not affect our results.

Table 2
Parameters and Their Priors or Constraints in ΛCDM or MOND

Parameter	Free?	Prior or Constraint	
Stars and BH		ΛCDM	MOND
$\Upsilon_{\star 0}$	free	>0	
K	free	[0, 1.5]	
β_0	free	[−2, 0.7]	
β_∞	free	[−2, 0.7]	
$r_a/R_{\rm e}$	free	[0.1, 1]	
$M_{\rm BH}$	constrained	$M_{\rm BH}$–$\sigma_{\rm e}$ relation[a]	
DM halo			
α	free	[0.1, 1]	
M_{200}	constrained	Table 1	
c_{200}	constrained	Equation (13)	
MOND IF			
ν[b]	free		[0.1, 2]
(or λ[c])			(or [0.3, 1.7])
a_0 [10^{-10} m s^{-2}]	free		[0.5, 1.9]

Notes.
[a] See Chae et al. (2018).
[b] MOND IF given by Equation (4).
[c] MOND IF given by Equation (5).

Thus, in practice, for each ATLAS$^{\rm 3D}$ galaxy, the two observed profiles $\sigma_{\rm los}(R)$ and $I(R)$ constrain three unknown functions of scale: $\Upsilon_\star(R)$, $\rho_{\rm X}(r)$, and $\beta(r)$. (Strictly speaking, the unknown is $\Upsilon_\star(r)$, but it is more convenient to consider the projected profile instead—for reasons that shall soon become clear.) Therefore, our approach is to adopt well-motivated, flexibly parameterized models for the three unknown profiles.

2.3. Model Parameterization

For the projected stellar mass-to-light profile, we set

$$\Upsilon_\star(R) = \Upsilon_{\star 0} \times \max\{1 + K[A - B(R/R_{\rm e})], 1\}, \quad (10)$$

with $A = 2.33$ and $B = 6$ (Bernardi et al. 2018; Chae et al. 2018). (We show that our results are robust to reasonable changes in these values in Section 5.) The "gradient strength" parameter K accounts for recent evidence of radial gradients in the central regions ($<0.4R_{\rm e}$) (e.g., Martín-Navarro et al. 2015; van Dokkum et al. 2017; Sonnenfeld et al. 2018). We allow $0 \leqslant K < 1.5$, as this includes the full range of gradient strengths reported in the literature.

For the velocity dispersion anisotropy, we use a generalized Osipkov–Merritt (gOM) model:

$$\beta_{\rm gOM}(r) = \beta_0 + (\beta_\infty - \beta_0)\frac{(r/r_a)^2}{1 + (r/r_a)^2} \quad (11)$$

(Binney & Tremaine 2008, p. 297), with allowed prior ranges $-2 < \beta_{\rm gOM}(r) < 0.7$ for all r and $0 < r_a < R_{\rm e}$, following Chae et al. (2018).

Finally, we must specify a model for $a_{\rm X}(r)$. In ΛCDM, we compute it by setting $\rho_{\rm X}$ equal to

$$\rho_{\rm gNFW}(r) \propto r^{-\alpha}\left[1 + c_{200}\left(\frac{r}{r_{200}}\right)\right]^{-3+\alpha}. \quad (12)$$

This is known as a generalized Navarro et al. (1997) model (hereafter gNFW). Here, r_{200} is the radius of the sphere within which the DM density is 200 times the cosmic mean matter density, α is the inner slope, and the outer slope is 3. Integrating this over a sphere of radius r yields $M_{\rm DM}(r)$ and hence $a_{\rm DM}(r) = GM_{\rm DM}(r)/r^2$. We allow $0.1 < \alpha < 1.8$ (the NFW value is $\alpha_{\rm NFW} = 1$). The halo mass $M_{200} \equiv M_{\rm DM}(r_{200})$ is constrained using the weak lensing derived $M_\star^{\rm Krou}$–M_{200} relation given in Table 1 (taken from Mandelbaum et al. 2016), where $M_\star^{\rm Krou}$ is the stellar mass derived assuming the Kroupa IMF (Kroupa 2002). The concentration parameter c_{200} is free, in principle, but we impose the constraint (Mandelbaum et al. 2008, 2016) that the outer profile $r > 0.2r_{200}$ mimics the NFW profile seen in N-body simulations. Then, following Section 3.3.1 of Chae et al. (2014), we set

$$c_{200} = \max\left[\left(\frac{3-\alpha}{2}c_{\rm NFW}(M_{200}) + \frac{1-\alpha}{9}r_{200}\right), \delta\right], \quad (13)$$

where $c_{\rm NFW}(M_{200}) = 7.192\,(M_{200}/(10^{14}M_\odot/h))^n$ with $n = 0.114 \pm 0.15$ (Diemer & Kravtsov 2015) and an arbitrary small $\delta > 0$. We also consider the Einasto profile (Einasto 1965) instead of the gNFW profile, as described in Chae et al. (2019).

For MOND, we simply use the relation $a_{\rm X}(r)/a_{\rm B}(r) = f - 1$ (Equation (3)), and we study a variety of choices for a_0 and the functional form of f (Equations (4)–(6)). The parameters in ΛCDM or MOND and their priors/constraints are summarized in Table 2.

We noted in the Introduction that the RAR carries qualitatively different implications for ΛCDM than for MOND. Therefore, in what follows, we first determine the RAR by using the Jeans equation to explain the observed line-of-sight velocity dispersion in the ΛCDM paradigm. We then follow the usual practice of asking what MOND IF best mimics the estimated dependence of $a_{\rm X}/a_{\rm B}$ on $a_{\rm B}$. However, we then repeat the entire analysis under the MOND paradigm. This second step is novel.

3. Results: The RAR in ΛCDM

In this section, we use a Bayesian approach (see, e.g., Wall & Jenkins 2012) to estimate the PDFs of the free parameters of a given model in ΛCDM. The free and constrained parameters are summarized in Table 2. The constrained parameters are, in principle, sampled in advance for each galaxy. We will consider two methods of MC sampling as described below in Section 3.1. In one method, for an efficient sampling, we will treat the constraint on M_{200} (Table 1) as a datum to be included in a likelihood function, and then treat M_{200} as a free parameter.

3.1. Bayesian Analysis of ATLAS^{3D} $\sigma_{\rm los}(R)$

Let $\boldsymbol{\Theta}$ denote the vector of free parameters associated with a model: e.g., for the gNFW model, $\boldsymbol{\Theta} \equiv (\Upsilon_{\star 0}, K, \beta_0, \beta_\infty, r_a, \alpha, (M_{200}))$. We then define

$$\chi^2(\boldsymbol{\Theta}) \equiv \sum_{i=1}^{N_{\rm bin}} \frac{[\sigma_{\rm los}^{\rm obs}(R_i) - \sigma_{\rm los}^{\rm mod}(R_i;\boldsymbol{\Theta})]^2}{s_i^2} \left(+ \frac{[\log_{10} M_{200} - \log_{10} M_{200}^{\rm WL}]^2}{s^2_{\log_{10} M_{200}}} \right), \quad (14)$$

where $\sigma_{\rm los}^{\rm obs}(R_i)$ is the measured velocity dispersion with its uncertainty s_i at R_i and $\sigma_{\rm los}^{\rm mod}(R_i;\boldsymbol{\Theta})$ is the value predicted by the model under consideration when the model parameters are $\boldsymbol{\Theta}$. The last term (in round parenthesis) in Equation (14) in only included if M_{200} is treated as a free parameter. Note here that $M_{200}^{\rm WL}$ denotes the weak lensing constrained value given in Table 1.

It is common to use this χ^2 to define a likelihood. We consider two likelihoods: one is the commonly adopted Gaussian likelihood given by

$$\mathcal{L}_{\rm Gaussian}(\boldsymbol{\Theta}) \propto \exp(-\chi^2(\boldsymbol{\Theta})/2). \quad (15)$$

In Bayesian inference, this likelihood, along with the prior assumptions about the range over which the parameters $\boldsymbol{\Theta}$ can be varied, is then used to generate MC samples (see, e.g., Allison & Dunkley 2014) of the posterior distribution, which is the product of the prior and the likelihood. We use a public Markov Chain Monte Carlo (MCMC) sampler "emcee," which is an implementation of the affine-invariant ensemble sampler by Foreman-Mackey et al. (2013), to generate draws from this posterior distribution. In principle, this provides the Bayesian inference of the posterior PDF of any of our free parameters or calculable quantities (e.g., $a_{\rm X}/a_{\rm B}$). Note that the posterior PDF returned by the emcee code, in general, differs from a Gaussian shape (i.e., Equation (15)) although we use flat priors for the free parameters (Table 2).

Although the likelihood given by Equation (15) is widely used to infer posterior PDFs, there is no guarantee that an MCMC sampling based on it will produce an unbiased result for our RAR problem, i.e., constraining the ratio $a_{\rm X}/a_{\rm B}$ as a function of $a_{\rm B}$. In fact, our test of the MCMC sampling using mock velocity dispersion profiles indicates that the Gaussian likelihood can produce too narrow a posterior distribution and thus may be vulnerable to biases in some cases (see Appendix A for details).

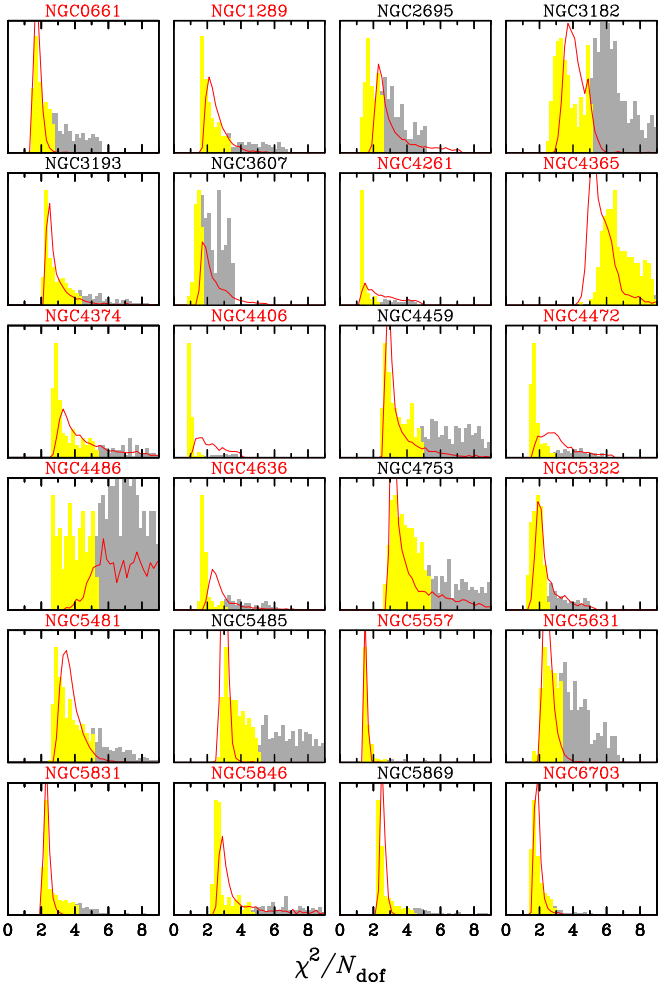

Figure 2. PDFs, from the SMC sampler, of the reduced χ^2, i.e., χ^2 (see Equation (14)) per $N_{\rm dof}$ (degree of freedom) when fitting a model that has a gNFW DM halo (Equation (12)). Yellow regions show $\bar{\chi}^2 < 2\bar{\chi}^2_{\rm min}$, while the gray regions are for $2\bar{\chi}^2_{\rm min} \leqslant \bar{\chi}^2 < 4\bar{\chi}^2_{\rm min}$. Red curve in each panel shows the posterior $\bar{\chi}^2$ distribution obtained from the MCMC sampler. Each red curve has been normalized so that the area under it matches the area under the corresponding yellow histogram. In this and the following figures, slow rotators are named in red unless noted otherwise.

Therefore, we also consider a simplistic "likelihood" given by

$$\mathcal{L}_{\rm TopHat}(\boldsymbol{\Theta}) \propto \begin{cases} 1 & \text{if } \bar{\chi}^2(\boldsymbol{\Theta}) < \bar{\chi}^2_{\rm crit} \\ 0 & \text{else,} \end{cases} \quad (16)$$

where $\bar{\chi}^2 \equiv \chi^2/N_{\rm dof}$ ($N_{\rm dof} = N_{\rm bin} - N_{\rm free}$) and $\bar{\chi}^2_{\rm crit}$ is a critical value that we define shortly. Compared to Equation (15), this does not penalize models (based on χ^2) that provide worse fits: they are either acceptable or not. We call this the Simple Monte Carlo (hereafter SMC) method. In this case, using a code written by one of us, we search the entire parameter space robustly. Further, all constrained parameters including M_{200} are sampled separately, and thus the last term in Equation (14) is not necessary. We note that the associated posterior PDF does not have a top-hat shape (even though the likelihood is effectively top-hat and the priors are uniform), because only certain combinations of parameters are accepted by Equation (16) and the PDF of $\bar{\chi}^2$ within these accepted models is not a top-hat shape. In general, the SMC method will lead to

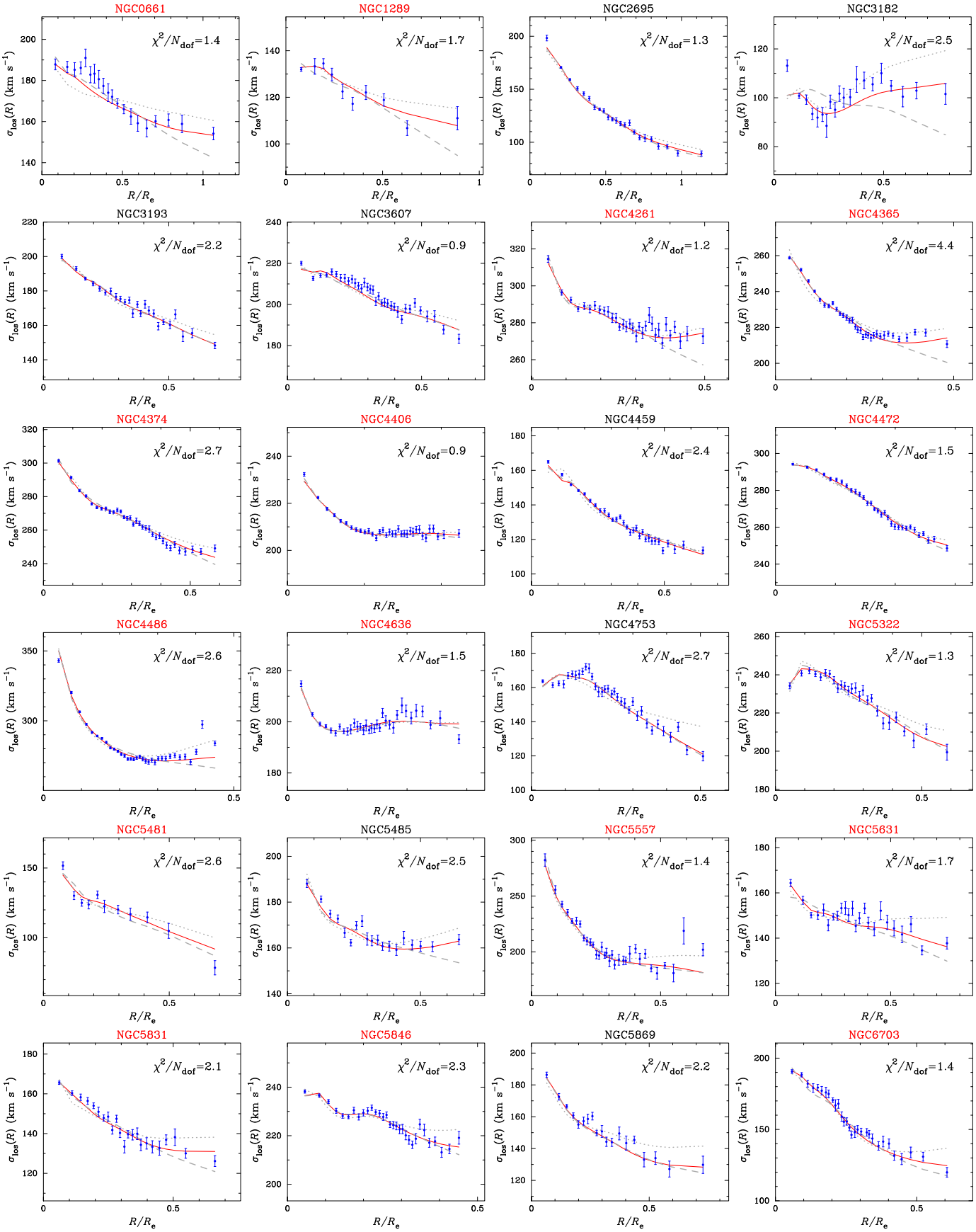

Figure 3. Observed line-of-sight velocity dispersion profiles (symbols). Smooth red curves show the best-fit models in which the DM halo is the gNFW of Equation (12). Gray dotted and dashed curves show the models that give rise to the upper- and lower-most RARs in Figure 6.

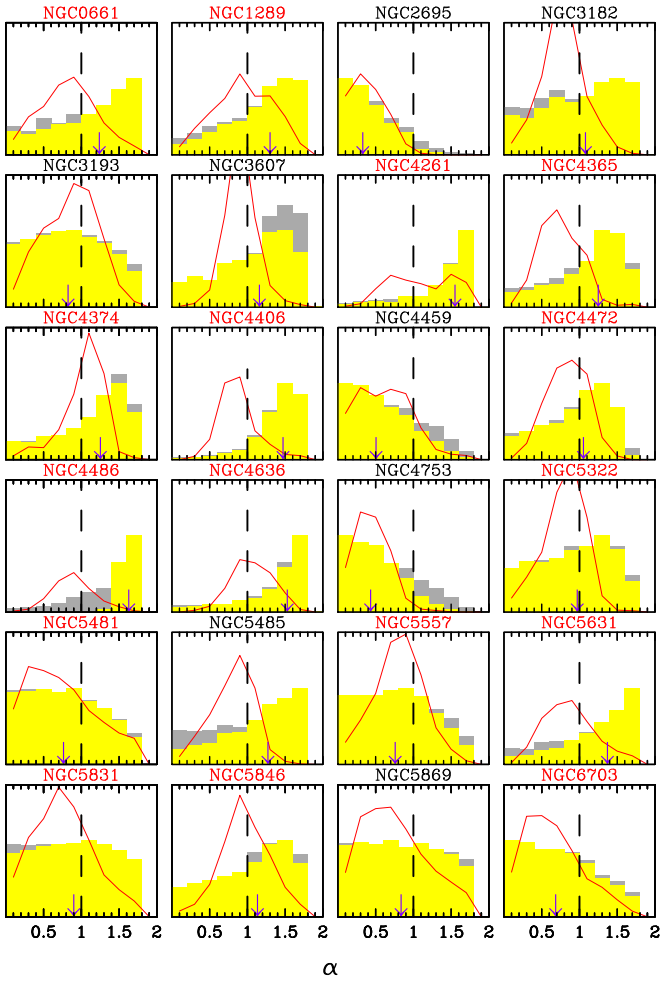

Figure 4. Posterior PDFs of the gNFW parameter α (Equation (12)) profile from the SMC sampling of models that resulted in Figures 2 and 3. Yellow regions represent models with $\bar{\chi}^2 < 2\bar{\chi}^2_{\rm min}$ and gray regions represent $2\bar{\chi}^2_{\rm min} \leqslant \bar{\chi}^2 < 4\bar{\chi}^2_{\rm min}$. Black dashed vertical line corresponds to the NFW profile ($\alpha = 1$), and the downward-pointing arrows indicate the median values. Red curves show the corresponding distributions returned by the MCMC sampler.

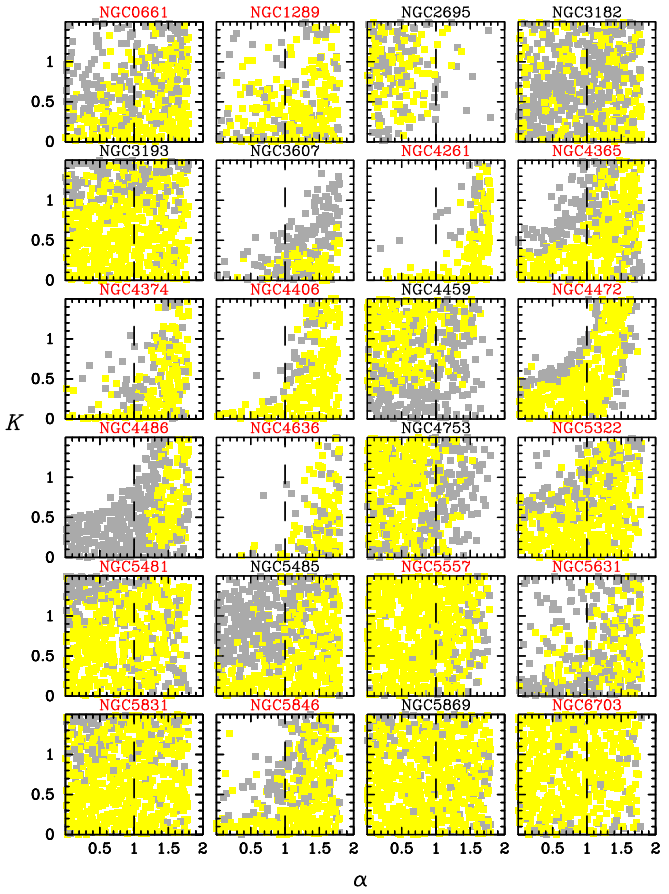

Figure 5. Correlation of α with K from our SMC sampler: yellow squares represent models with $\bar{\chi}^2 < 2\bar{\chi}^2_{\rm min}$, while the gray squares represent $2\bar{\chi}^2_{\rm min} \leqslant \bar{\chi}^2 < 4\bar{\chi}^2_{\rm min}$. In many cases, α increases when K increases, but the opposite does not occur. Appendix B shows the full correlation of all parameters derived from the MCMC sampler for the four roundest galaxies.

a broader posterior—and hence to less restrictive constraints—compared to the $\mathcal{L}_{\rm Gaussian}$-based MCMC method. In Section 4.1, we verify that the SMC method produces robust RAR results in the MOND framework (see also Appendix A).

Figure 2 shows the posterior distributions of $\bar{\chi}^2$ based on the two MC sampling methods. The red curve in each panel shows the distribution obtained from the MCMC sampler. The yellow histograms show models satisfying $\Delta\bar{\chi}^2 = \bar{\chi}^2 - \bar{\chi}^2_{\rm min} < \bar{\chi}^2_{\rm min}$ (where $\bar{\chi}^2_{\rm min}$ refers to the global minimum value from our SMC search), i.e., use $\bar{\chi}^2_{\rm crit} = 2\bar{\chi}^2_{\rm min}$ in Equation (16). Because $\bar{\chi}^2_{\rm min} \lesssim 2.5$ for most galaxies, this means that the probability $P(\Delta\bar{\chi}^2 > \bar{\chi}^2_{\rm min})$ would be $\gtrsim$0.001 for Gaussian statistics. This is a normally accepted criterion, and our numerical experiments using mock velocity dispersion profiles also suggest that this is a reasonable choice (see Section 4.1 and Appendix A). However, we will also consider a relaxed criterion of $\bar{\chi}^2_{\rm crit} = 4\bar{\chi}^2_{\rm min}$ (gray regions) to see the effect of varying $\bar{\chi}^2_{\rm crit}$. When we derive a statistically weighted RAR using all galaxies in Section 3.6, we will see that both choices of $\bar{\chi}^2_{\rm crit}$ give similar results (although individual RARs can be broader with $\bar{\chi}^2_{\rm crit} = 4\bar{\chi}^2_{\rm min}$ in some galaxies).

The difference between the red curve and the shaded region in each panel of Figure 2 illustrates how badly a model can fit the data and still be accepted by our two methods. Therefore, as a sanity check, Figure 3 compares the observed $\sigma_{\rm los}(R)$ profiles (symbols) with the gNFW models having $\chi^2_{\rm min}$. Notice that the profiles that rise slightly at larger R (i.e., NGC 3182, 4365, 4486) tend to be harder to fit (they have broader $\bar{\chi}^2$ distributions). The gray dotted and dashed curves show fits that give rise to the upper- and lowermost RARs in Figure 6.

3.2. Implications for Halo Profiles

Because an MC set automatically defines a distribution of models (i.e., correlated distribution of free parameters), we can calculate the PDF of any quantity of interest. Posterior distributions of stellar mass and K based on our SMC sets can be found in Chae et al. (2018), while those of the velocity dispersion anisotropy profiles can be found in Chae et al. (2019). In those papers, we show that whenever an appropriate comparison is possible, our results agree well with independent literature results.

Figure 4 shows the distribution of the gNFW-profile parameter α from our SMC sampling of the 24 ATLAS^{3D} galaxies (gray histograms). Red curves show the corresponding

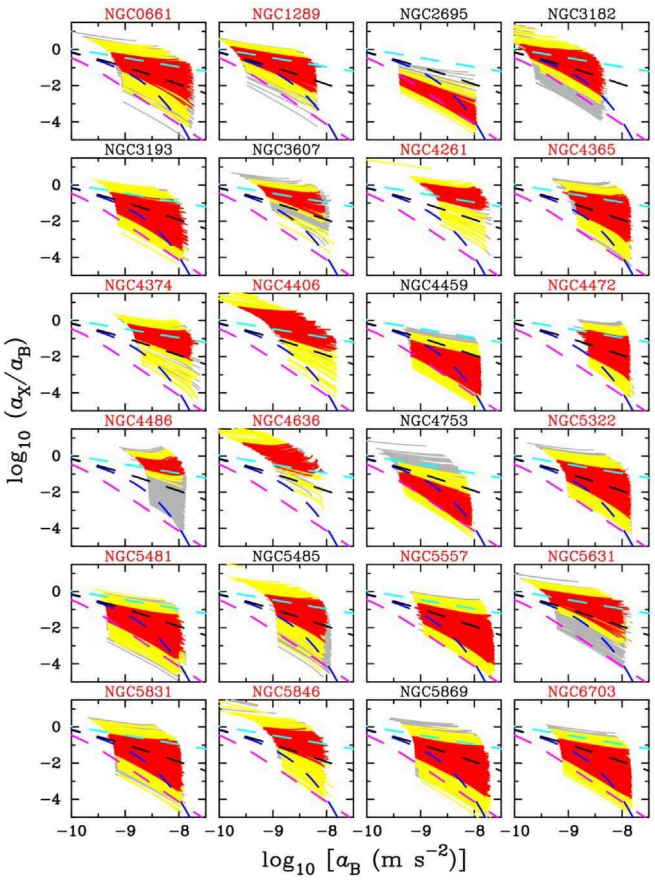

Figure 6. Individual radial acceleration relation for 24 pure-bulge ATLAS^{3D} galaxies when the DM component is assumed to follow the gNFW profile (Equation (12)). Each colored line represents the radial behavior of the ratio $a_X(r)/a_B(r)$ from one model in the MC set. Yellow curves show cases that have $\tilde{\chi}^2 < 2\tilde{\chi}^2_{\rm min}$; gray curves represent $2\tilde{\chi}^2_{\rm min} \leqslant \tilde{\chi}^2 < 4\tilde{\chi}^2_{\rm min}$. Red curves represent the region that contains 68% of the yellow lines. Thick colored dashed curves are the same functions shown in Figure 1.

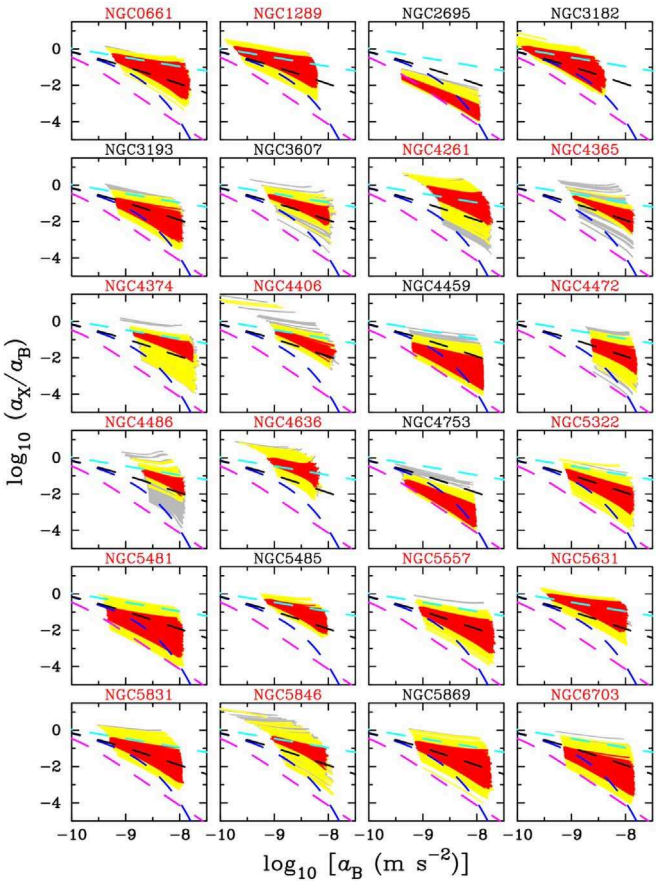

Figure 7. Same as Figure 6, but from the MCMC sampling.

MCMC posteriors. Figure 5 shows that its value is correlated with that of the $\Upsilon_\star$-gradient parameter K: when K increases, α also tends to increase. The median value of α tends to be close to unity, suggesting that the simple NFW profile (as opposed to gNFW) is close to the median DM halo profile of elliptical galaxies. This is qualitatively consistent with recent results based on combined analyses of strong lensing and stellar kinematics (Sonnenfeld et al. 2015; Shankar et al. 2017).

3.3. Implications for the RAR

Let us directly consider our main question: what do our MC models imply for the RAR? This question in ΛCDM now appears to be particularly interesting because the median property of the constrained DM halo has been shown to be close to the NFW. Figure 6 shows the distribution of the acceleration ratio $a_X(r)/a_B(r)$ from the SMC models for each of the 24 ATLAS^{3D} galaxies. The red curves are associated with model parameters that describe the observed $\sigma_{\rm los}(R)$ best. Yellow curves are slightly worse, and the gray curves have model parameters that provide poor descriptions of $\sigma_{\rm los}(R)$. Note that these individual results are more reliable for SRs (galaxy names in red) because we are using spherical galaxy models. Despite the wide range of $\sigma_{\rm los}(R)$ shapes, the distribution of RAR shapes defined by the red curves is reasonably narrow. This is the motivation for the suggestion that the RAR must encode interesting physics. In the context of ΛCDM, this must constrain the physics of how these galaxies formed.

Figure 7 shows the results from the MCMC sampling for the same model of the DM halo, i.e., the gNFW profile. Compared with the SMC results, the individual RARs are more narrowly distributed because the MCMC uses a Gaussian likelihood. If we use the Einasto profile for the DM halo (instead of the gNFW) whose parameterizations and priors are described in Chae et al. (2019), then we obtain essentially the same results. Clearly, the RAR is not sensitive to the differences between these two descriptions of DM halos.

3.4. Implications for MOND

The RARs in ΛCDM shown in Figures 6 and 7 represent correlations (or the correlation) between baryons and the assumed DM under Newtonian gravity and Newtonian dynamics. However, if the DM halo approach is interpreted as simply a parameterization of the kinematic data, and the resulting RAR is not biased by the choice of parameterization, then we can actually use the RAR from the DM approach to learn something about other approaches. In this respect, it is particularly interesting that the RAR is directly related to the IF in the MOND paradigm. As the exact shape of the IF is a critical open question in MOND, it is interesting to compare the individual RARs from the DM approach to various proposed

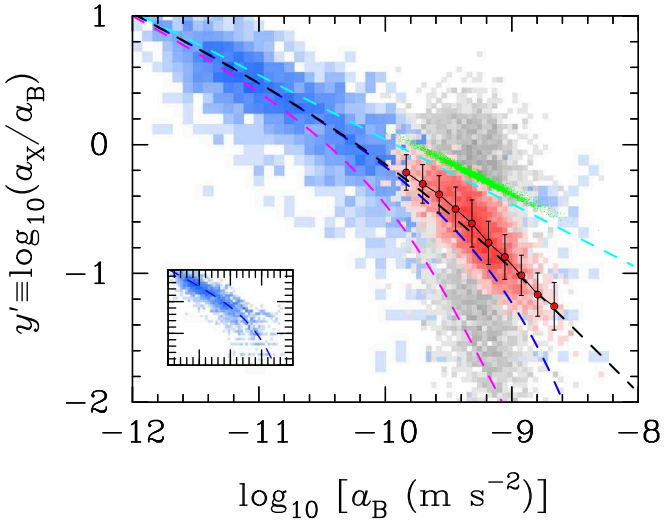

Figure 8. Gray pixels with varying intensity display the distribution of a_X/a_B at $r = R_{ap}$ as a function of $a_B(r = R_{ap})$ in one MC realization for 3991 SDSS galaxies for which modeling is successful with the standard input of (K_{max}, b') = (1, −0.18) and a gNFW DM halo. Red pixels with varying intensity represent the median values in the 90 MC realizations of the 3991 galaxies. Red-filled circles and error bars represent the mean and standard deviation of the medians within each bin of a_B. Colored dashed curves are the same as in Figure 1. Green points are predicted by Verlinde's emergent gravity. Blue pixels represent 2693 data points from rotating galaxies in the literature (Lelli et al. 2017), for which we use the proxy $a/a_B - 1$ for a_X/a_B. The inset reproduces these data points only.

RARs or MOND IFs shown by thick colored dashed curves in Figures 6 and 7. This is the way in which a Newtonian+DM–derived RAR is typically used. However, we will also consider self-consistent analyses of MOND in Section 4.

Recall that, if MOND is correct, there is a single universal RAR that must provide an acceptable description of all galaxies. That said, it appears that some galaxies (e.g., NGC 4406, 4486, 4636) disfavor the McGaugh IF while others (e.g., NGC 2695, 4459, 4753) disfavor the Bekenstein IF. On the other hand, it appears that the Simple IF does not have much difficulty in fitting any of the ATLAS^{3D} galaxies–except possibly for NGC 2695, which is however a fast rotator. If a single IF must describe all galaxies, then the results of this section suggest that only the Simple IF is a viable model. We discuss this further in Sections 3.6 and 4.4).

3.5. The Typical RAR from 4201 SDSS Galaxies

We now turn to the question of using the much larger sample of SDSS galaxies to estimate the RAR. For these galaxies, the procedure for obtaining an MC set with the single dynamical constraint (i.e., σ_{ap}: Equation (7)) necessarily differs from that for an ATLAS^{3D} galaxy for which $\sigma_{los}(R)$ is observed over a range of R.

For SDSS galaxies, the light distribution and DM halo parameters are drawn in the same way, but K is drawn from a range $0 \leqslant K < K_{max}$ where K_{max} is chosen so that the posterior distribution matches that for the ATLAS^{3D} galaxies. Then, $M_{\star e}$ is assigned using the fundamental mass plane (FMP) derived for the ATLAS^{3D} galaxies, a correlation of the effective radius R_e with the light-weighted mean line-of-sight velocity dispersion $\sigma_e \equiv \langle\sigma_{los}\rangle(R = R_e)$ and the projected stellar mass $M_{\star e}$, which is a function of K: $\log_{10} M_{\star e} = \log_{10} M_{\star e}(K) = \log_{10} M_{\star e}(K = 0) + b'K$ with $b' = -0.18^{+0.02}_{-0.07}$ (Chae et al. 2018). Finally, we search iteratively for a velocity dispersion anisotropy drawn randomly from a prior range (consistent with the ATLAS^{3D} galaxies; see Chae et al. 2019) predicting σ_{ap} within the estimated error.

In all, we generate a set of 90 MC models for each galaxy. If 68% of the models in the set match the observed σ_{ap} within the formal measurement error, we accept the set. Only about 200 galaxies fail this test: the vast majority, about 4000 galaxies, pass (see Chae et al. 2018 for further details). For each of these models, we estimate the values of a_X and a_B associated with the scale R_{ap}. From these, we generate posterior distributions of a_X and a_B.

Figure 8 exhibits the distribution of ∼4000 galaxies successfully modeled by SDSS in the plane spanned by a_B and a_X/a_B at $r = R_{ap}$ of the galaxies for the standard input (Chae et al. 2018) under the ΛCDM case with the gNFW halo profile (if the Einasto profile is used instead, we obtain very similar results). In this figure, we distribute MC models of the SDSS galaxies in pixels such that the intensity of each pixel indicates the occupancy of galaxies (i.e., a probability). Gray pixels represent one MC realization of the SDSS galaxies while red pixels represent the medians in the MC sets of the 90 realizations. The red pixels show that, in agreement with the results for the ATLAS^{3D} galaxies, the Simple RAR (black dashed curve) is most consistent with SDSS galaxies. Figure 8 also reproduces published results for mostly spiral galaxies (blue pixels). Note that blue pixels occupy mostly subcritical acceleration regions and are consistent with both the Simple and McGaugh's IFs but cannot distinguish them well in the supercritical regime.

3.6. The Stacked RAR

So far, we have obtained the distribution of MC models in the RAR plane for each of the 24 ATLAS^{3D} galaxies and ∼4000 SDSS galaxies (Figures 6–8). Figure 9 exhibits the outcome of statistically weighting all the individual results. We have obtained this as follows. First, because the typical acceleration scale in our sample is supercritical, we define $a_{+1} \equiv 10^{+1} \times (1.2 \times 10^{-10})\,\mathrm{m\,s^{-2}} = 1.2 \times 10^{-9}\,\mathrm{m\,s^{-2}}$, and express all accelerations in units of a_{+1}. We define 13 bins of $x' \equiv \log_{10}(a_B/a_{+1})$ in steps of 0.15 in the range $-1 < x' < 1$.

We then calculate a statistically weighted PDF of $y' \equiv \log_{10}(a_X/a_B)$ in each bin of x', using the SDSS (or ATLAS^{3D}) galaxies whose individual RAR results belong to (or have an overlap with) the x' bin. Note that an ATLAS-^{3D}galaxy spans multiple bins, while an SDSS galaxy belongs to one bin. Note also that ATLAS^{3D} galaxies occupy bins of higher x', while SDSS galaxies occupy lower x' (two middle bins are overlapped). For the ith SDSS (or ATLAS^{3D}) galaxy of the x' bin, we derive $dP_i(<y')/dy'|_{x'}$ using the models in the MC set (i.e., 90 MC realizations for each SDSS galaxy like the gray pixels as in Figure 8, or all curves for each ATLAS^{3D} galaxy as in Figure 6) that have x' in the desired range. Here, $P_i(<y')|_{x'}$ is the cumulative probability up to y' at x' (in the sense of $P_i(<\infty) = 1$) calculated numerically using the MC models of the galaxy. For the x' bin, we derive a statistically weighted ("stacked") PDF

$$\left.\frac{dP(<y')}{dy'}\right|_{x'} \propto \sum_i \left.\frac{dP_i(<y')}{dy'}\right|_{x'} w_i, \qquad (17)$$

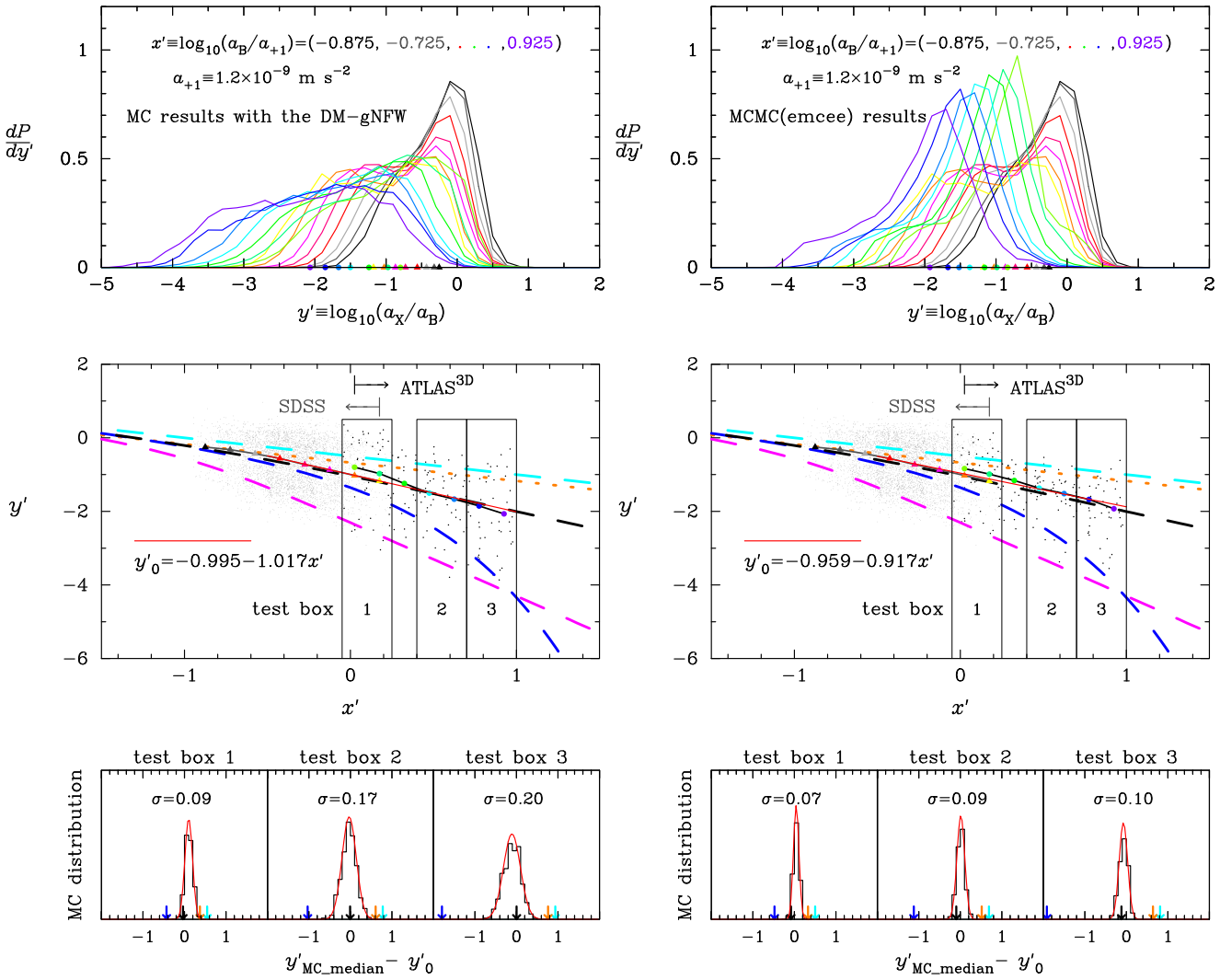

Figure 9. Top left panel shows PDFs (Equation (17)) of y', numerically constructed in the bins of x' centered at $x' = -0.875, -0.725, \cdots, 0.925$, based on the MC results with the gNFW DM halo profile (Equation (12)) through the SMC sampling. Color-filled circles (triangles) show medians of the PDFs of the ATLAS^{3D} (SDSS) galaxies. Middle panels illustrate the stacked RAR (correlation of y' with x'). Small dots show one MC realization for the considered bins of x' based on the PDFs of the top panel. Colored circles and triangles show the medians in the bins of x' displayed in the top panel. Red line shows a linear fit to the points in the range $-0.5 < x' < 1$. Thick colored dashed curves show the same IFs as in Figure 1, with $a_0 = 1.2 \times 10^{-10}$ m s^{-2}. The orange dotted curve represents the ΛCDM prediction from van Putten (2018). In the bottom panels, we show the distribution of the median of MC realizations that lie in the three test boxes labeled in the middle panel. Red curve is a Gaussian fit to the histogram with the standard deviation indicated by σ. Downward-pointing arrows indicate the predictions by the colored dashed/dotted curves at the relevant value of x'. Right panel is the same as the left, but through the MCMC sampling.

where $P_i(<y')|_{x'}$ is the individual PDF of ith galaxy and w_i is the statistical weight assigned to that PDF. We have tried $w_i = 1$ (i.e., uniform weighting) and $w_i = \exp(-\bar{\chi}^2_{{\rm min},i}/2)$, where $\bar{\chi}^2_{{\rm min},i}$ is the minimum value of the reduced χ^2 for the galaxy. Although this second weighting scheme accounts for the fact that some MC realizations provide much better descriptions of the measured $\sigma_{\rm los}(R)$ than others, it turns out that both weighting factors give very similar results.

The top panels of Figure 9 show the stacked PDFs of y' for a number of bins in x' (as labeled) when $w_i = \exp(-\bar{\chi}^2_{{\rm min},i}/2)$. The triangles and circles along the x-axis of these top panels show the medians of these PDFs based on SDSS and ATLAS^{3D} galaxies, respectively. The middle panels show the result of plotting these median values versus x', and constitute our estimate of the "stacked" RAR associated with gNFW DM halo profiles based on the SMC sampling (left) or the MCMC sampling (right) in the ΛCDM paradigm. Over the acceleration scales where they overlap, there is reasonable agreement between our SDSS and ATLAS^{3D} samples. Moreover, the estimated RAR does not depend strongly on whether we parameterize the DM distribution using a gNFW or Einasto profile.

The dots in the middle panel show x' and y' values for one MC realization of each of the ATLAS^{3D} and SDSS galaxies: i.e., each ATLAS^{3D} galaxy contributes seven (number of the x' bins) dots, whereas each SDSS galaxy contributes only one. The filled triangles and circles show the median values obtained from the top panels for the two samples.

3.7. Implications for ΛCDM and MOND from the Stacked RAR

Having estimated the empirical RAR from a Newtonian analysis, we now compare it with various predictions/

suggestions, including the ΛCDM prediction and MOND-related predictions. The philosophy here is that the RAR, if derived robustly from the kinematic data through any approach, may provide a useful constraint on any other approach. We do this in two ways. First, we simply overplot the same four MOND IFs, using thick dashed curves, as in previous figures. Recall that differences between the curves cannot be attributed to reasonable changes in a_0 (see Figure 1). The thick dotted orange curve shows a prediction for ΛCDM taken from van Putten (2018); it is quite similar to Bekenstein's IF (cyan). It is clear that the Simple and McGaugh IFs (black and blue curves) and the ΛCDM prediction (orange dotted curve) agree below $10^{0.5}a_{+1}$ and provide good descriptions of our empirically determined RAR up to $\sim a_0$ probed by our SDSS galaxies. However, in the acceleration range dominated by ATLAS-^{3D}galaxies, the Simple IF provides a better description than the others.

Our second way of demonstrating this is as follows. For the probed range $-1 < x' < 1$, the points defining the RAR cannot be described by a linear relation; some curvature is evident in the middle panels of Figure 9. However, for the range $-0.5 < x' < 1$, we may approximate the RAR by a linear fit of $y' = p + q\,x'$ with $p = -1.00 \pm 0.03$ and $q = -1.02 \pm 0.09$ (the SMC case), or $p = -0.96 \pm 0.02$ and $q = -0.92 \pm 0.06$ (the MCMC case), where the statistical uncertainties have been estimated using a number of Monte Carlo realizations based on the PDFs of the top panels. Although we do not show so explicitly, the result with Einasto DM halo profiles is very similar with $p = -1.07 \pm 0.03$ and $q = -0.99 \pm 0.10$ (Einasto, the SMC case).

The bottom panels show examples of the Monte Carlo distributions for three narrow ranges of x'. One of them (test box 1) uses four PDFs (two from the ATLAS^{3D} galaxies and the other two from the SDSS galaxies) within the range of x' while each of the other two (test box 2 and 3) uses two PDFs from the ATLAS^{3D} galaxies within the respective range of x'. Downward-pointing arrows indicate the predictions of the IFs represented by the colored dashed curves at the relevant value of x'. Both the linear fit for $-0.5 < x' < 1$ and the three test boxes clearly prefer the Simple RAR indicated by the black dashed curve in the middle panel and black downward-pointing arrows in the test boxes. As the RAR determined from the data used Newtonian physics, the next section provides a fully self-consistent check of the conclusion that the Simple RAR provides the best fit of the MONDian IFs we have considered.

However, it is fair to explore the discrepancy between the RAR and ΛCDM model represented by the orange dotted line. The orange arrows in the bottom panels (see test boxes 2 and 3) of Figure 9 suggest that it is not consistent with our data. This may seem contradictory, as our analysis was done within the ΛCDM framework. The point is that this ΛCDM "prediction" depends on the assumed astrophysics of galaxy formation (represented, in this case, by the MUGS simulations analyzed by van Putten 2018). The mismatch here suggests that the RAR provides an interesting complementary test of the physics of galaxy formation.

Finally, we point out that Figure 8 shows a comparison of the gNFW-based RAR we have determined for ellipticals with that for spirals. While the spiral galaxies data can be well described by either the McGaugh IF or the Simple IF, the elliptical galaxies can only be described by the Simple IF. This highlights the gain that comes from studying the supercritical regime with elliptical galaxies.

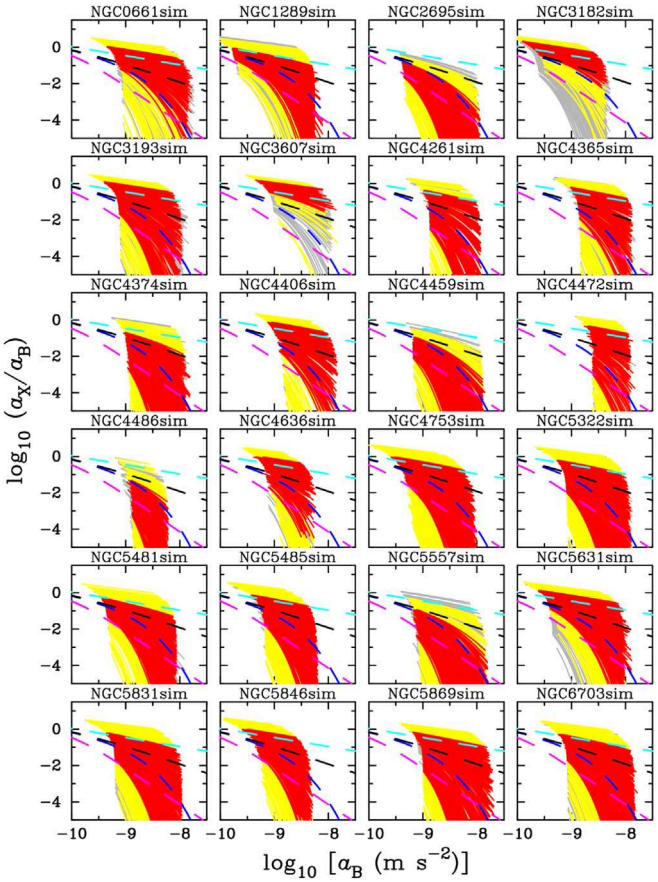

Figure 10. Individual RARs derived from the mock McGaugh IF (Equation (5) with $\lambda = 1$) $\sigma_{\rm los}(R)$ profiles by our SMC analysis in which λ and a_0 are free parameters.

4. Results: The RAR in MOND

The previous section presented a Bayesian analysis of $\sigma_{\rm los}(R)$ in elliptical galaxies, assuming Newtonian accelerations and parametric models for the DM profile. Comparison of the resulting RAR with several MOND IFs suggested that the Simple IF (Equation (4) with $\nu = 1$) provides a good description. Here, we provide a complementary analysis of the same data, performed entirely within the MOND framework. This means that, instead of the parameters associated with the DM halo (α, etc.), we work with the parameters of the IF (Equation (4) or (5)): a_0 and ν or λ.

4.1. Verification of Methodology Using Mock Profiles

In principle, the "free parameters" in MOND are not analogous to those of the DM, because a given (a_0, ν) or (a_0, λ) pair must work for all galaxies. (In contrast, there is no requirement that α be the same for all galaxies in the gNFW DM halo.) Therefore, although it is straightforward to run our Bayesian analysis pipeline with a_0 and λ or ν left as free parameters, it is not obvious what the results will mean.

To address this, we use the observed light profiles and the estimated K and velocity dispersion anisotropy parameters (from modeling real $\sigma_{\rm los}(R)$ profiles). We then set (λ, a_0) = (1,

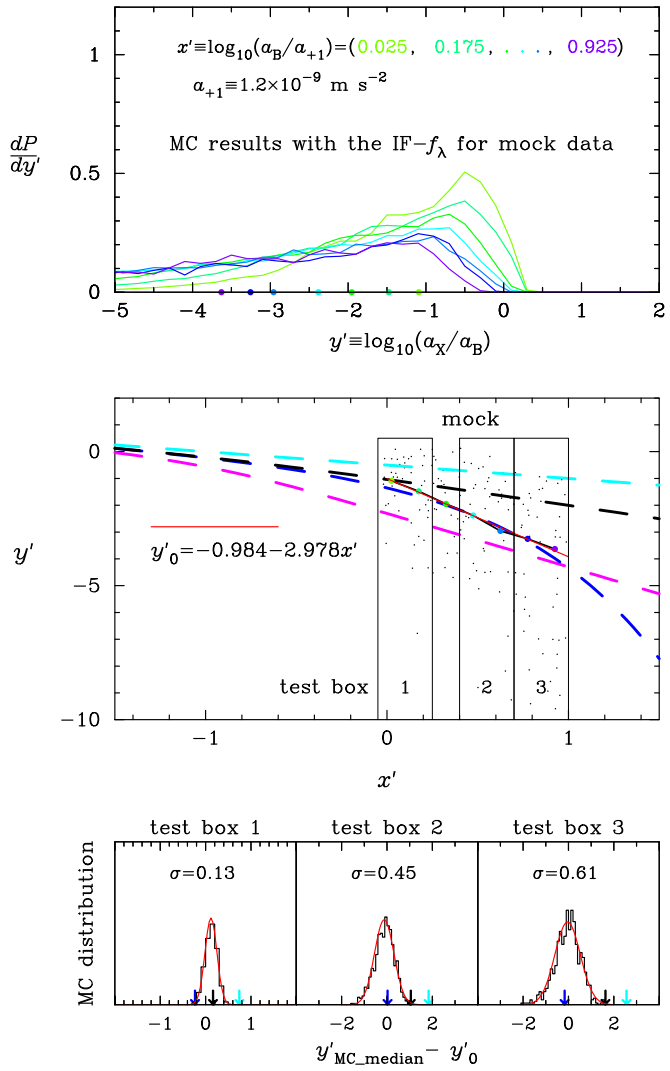

Figure 11. Stacked RAR determined from our analysis of the mock $\sigma_{los}(R)$, shown in the same format as Figure 9. SDSS data are not included here, because we are considering mock data only.

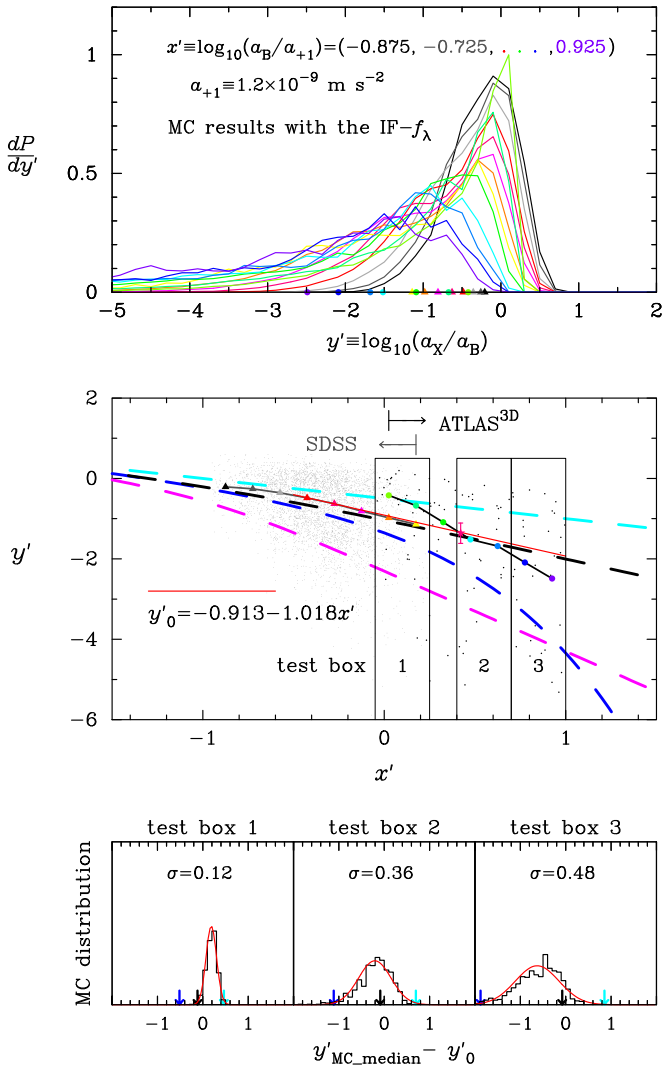

Figure 12. Same as Figure 11, but for the ATLAS^{3D} $\sigma_{los}(R)$: i.e., stacked RAR assuming the MOND IF is given by Equation (5) with the parameters λ and a_0 allowed to vary from one galaxy to another. The pink star with an error bar is the mean of the 24 best-fit models at $x'=0.42$ based on f_γ (Equation (6)), which provides a robust test of the Bekenstein (cyan) IF (see the text).

$1.2\times10^{-10}\,\mathrm{m\,s^{-2}}$) to generate velocity dispersions, which we project, and then add noise to get a mock $\sigma_{los}(R)$. By choosing these values of (λ, a_0), we have ensured that our set of mock profiles will represent plausible observations if the McGaugh IF is correct for all galaxies. We then run the Bayesian analysis pipeline, leaving (λ, a_0), Υ_{*0}, K, and anisotropy parameters as free, and treating this mock $\sigma_{los}(R)$ as the data. If the analysis pipeline is unbiased, it should recover the input (λ, a_0).

Figures 10 and 11 show the results through the SMC sampling. Individual RARs (distributions of the SMC models in the a_B–a_X/a_B plane) are statistically consistent with the input McGaugh IF. That is to say, for all 24 cases, the McGaugh IF is within the yellow regions defined by our acceptance criterion $\bar{\chi}^2<2\bar{\chi}^2_{min}$, and for over two-thirds of cases, the McGaugh IF is within the 68% confidence region (red). Furthermore, the stacked RAR based on the stacked PDFs of y' as a function of x' clearly recovers the McGaugh IF without any bias. In particular, the middle panel of Figure 11 shows that the stacked RAR is centered on the McGaugh IF, and the bottom panel "rules out" the Simple IF. This suggests that, if there is a universal RAR and it has a functional form that is similar to the MOND IFs, then our Bayesian analysis, in which we allow the parameters of the IF to vary from one object to another, will return an RAR that is close to the true universal one.

We have also obtained MCMC results using the code emcee for the mock velocity dispersions (see Appendix A). The MCMC results provide narrower (more precise) regions in the RAR space compared to SMC—but in some cases, the "precise regions" exclude the McGaugh IF even though it is the correct answer. This means that the emcee code sometimes produces unrealistically narrow constraints. With this caveat in mind, we will present mainly the results from the SMC sampling for the real data in the MOND framework. However, it turns out that both sampling methods give consistent results, albeit with the rule of thumb that those of the MCMC sampling are narrower.

4.2. The Stacked RAR

With this in mind, we run our Bayesian SMC analysis pipeline on the ATLAS^{3D} $\sigma_{los}(R)$ profiles, allowing both the MOND IF profile index λ and the critical acceleration a_0 to be

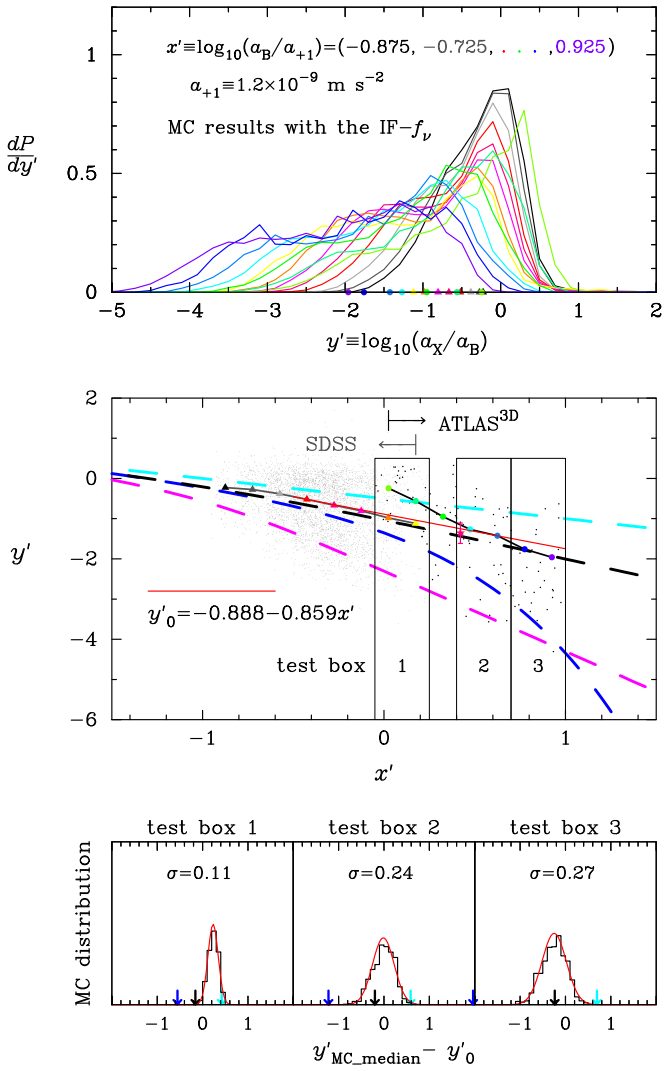

Figure 13. Same as Figure 12, but with the MOND IF given by Equation (4) with parameters ν and a_0 allowed to vary from one galaxy to another.

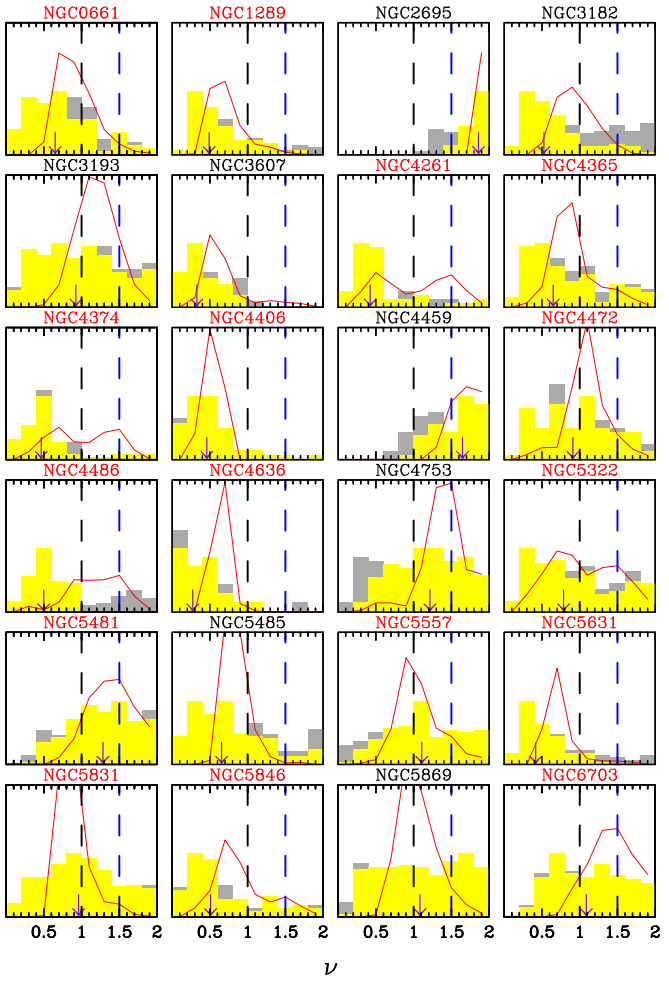

Figure 14. Posterior PDFs of ν for the f_ν-IF (Equation (4)) from the models satisfying $1.0 < a_0 < 1.4$ (in units of 10^{-10} m s^{-2}). Yellow (or gray) histograms represent the PDFs returned by our SMC sampling with $\bar{\chi}^2 < 2\bar{\chi}^2_{\rm min}$ (or $\bar{\chi}^2 < 4\bar{\chi}^2_{\rm min}$). Downward-pointing arrows indicate the medians of the yellow histograms. Red curves show the PDFs returned by the MCMC sampling. The black dashed vertical line corresponds to the Simple IF, while the blue line corresponds to the closest match to the McGaugh IF in this parameterization.

free parameters within specified prior ranges: $0.3 < \lambda < 1.7$ and $0.5 < (a_0/10^{10}\,{\rm m\,s^{-2}}) < 1.9$. We then obtain the ratio $a_X(r)/a_B(r)$ using the MC models of each galaxy, and combine them to produce a stacked RAR. Figure 12 exhibits the results. The middle and bottom panels show that McGaugh's IF is not picked out by the stacked RAR; the Simple IF is clearly favored.

Because the Simple IF is a special case of Equation (4) rather than (5), Figure 13 shows the result of repeating the entire analysis, but using Equation (4) as the IF. In this case, we allow the same prior range in a_0, but allow $0 < \nu \leqslant 2$. Not only is the Simple IF again preferred, but the distributions shown in the bottom panel are narrower than they were in Figure 12 and more like those in Figure 9. This again suggests that the Simple IF is closer to the true RAR than is McGaugh's function.

For completeness, a linear fit of $y' = p + q\,x'$ over the range $-0.5 < x' < 1$ returns $p = -0.91 \pm 0.04$ and $q = -1.02 \pm 0.13$ in the f_λ case, and $p = -0.89 \pm 0.04$ and $q = -0.86 \pm 0.12$ in the f_ν case. These values are rather similar to those under the ΛCDM paradigm (Figure 9).

We have also considered using the model f_γ (Equation (6)) because it can allow a more direct test of Bekenstein's IF. The pink star with an error bar displayed in Figures 12 and 13 is the mean of the best-fit models of the 24 ATLAS^{3D} galaxies with f_γ. As our modeling of mock velocity dispersion profiles generated with Bekenstein's IF verifies that this quantity is robustly reproduced, this result also prefers the Simple IF over other IFs.

To sum up, in the supercritical acceleration regime probed by the nearly spherical ATLAS^{3D} and SDSS galaxies, the Simple IF is consistent with our stacked RAR, whereas Bekenstein's and McGaugh's IFs are not. For each of test boxes 2 and 3 in the bottom panels of Figures 12 and 13, the two IFs are excluded at $\sim3\sigma$ to $\sim9\sigma$ depending on the DM halo or MOND IF parameterization. This means that they are excluded at $\gtrsim4\sigma$.

4.3. Universality of the MOND Parameters

Although the Simple IF appears to provide a good description of the RAR, because ν and a_0 are supposed to be the same for all galaxies in the MOND paradigm, it is

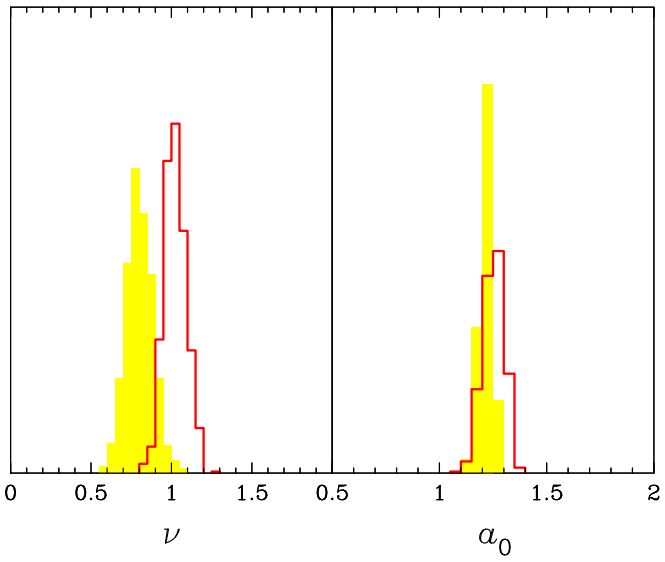

Figure 15. Monte Carlo distribution of "universal" values of ν (of the f_ν IF) and a_0 (in units of 10^{-10} m s^{-2}) for the 24 ATLAS^{3D} galaxies, based on a bootstrap resampling of individual medians shown in Figure 14. Yellow and red histograms show the SMC and MCMC results, respectively. Both are consistent with the Simple IF ($\nu = 1$) with $a_0 \approx 1.2$.

important to check whether the PDFs of ν and a_0 returned by our Bayesian analysis can support universality.

The issue of universality in rotating galaxies was recently discussed in the context of whether a_0 is universal for all galaxies for a fixed MOND functional form (Kroupa et al. 2018; McGaugh et al. 2018; Rodrigues et al. 2018). For such an analysis, the algorithm employed to infer the posterior PDF plays a critical role because the conclusion can depend on the width of the PDF. Here, we directly tackle the MOND functional form f_ν for a narrow range of $a_0 = (1.0, 1.4) \times 10^{-10}$ m s^{-2}. We intend to check whether $\nu = 1$ is indeed consistent with all galaxies.

Figure 14 exhibits the individual PDFs of ν through the SMC or MCMC sampling. Overall, the two samplers give qualitatively consistent results, but the MCMC PDFs are narrower—as expected. (We have already noted, in Section 4.1, that the MCMC results can sometimes be unrealistically narrow.) The individual PDFs of ν from the SMC typically include the Simple IF ($\nu = 1$), but exclude the McGaugh IF ($\nu = 1.5$) in several cases. If we limit our attention to the more reliable sample of 16 SRs, our results are clearly consistent with the view that the Simple IF is universal in the sample. Given this preliminary result, it will be interesting to see future results from analyses of much larger samples.

Accepting the view that there exists a universal IF in our sample, we now determine the "universal" values of ν and a_0 of the assumed f_ν function in our sample. In doing so, we treat each galaxy as one datum, and the median of the PDF (the downward-pointing arrow in each panel of Figure 14) represents a measured value of ν (and the width of the PDF represents the individual uncertainty). To determine the universal value and its uncertainty, we use a bootstrap resampling of the individual medians shown in Figure 14. We obtain the sample mean of each bootstrap sample, and the distribution of the sample means provides our estimate of the universal value. Figure 15 shows the results for ν and a_0. We obtain $\nu = 0.80 \pm 0.08$ and $a_0 = 1.24 \pm 0.04$ (based on the SMC results), or $\nu = 1.02 \pm 0.07$ and $a_0 = 1.25 \pm 0.05$ 10^{-10} m s^{-2} (based on the MCMC results). These results are in good agreement ($<2.4\sigma$) with the Simple IF ($\nu = 1$), as expected. The case of $\nu = 1.5$ as a proxy for the McGaugh IF is excluded at $>7\sigma$ by these results. Our determined value of a_0 is in good agreement with the commonly known value of $a_0 = 1.2$ or 1.3. Although we do not show it here, a similar result is obtained for λ of the f_λ IF (Equation (5)).

4.4. Eliminating Models by Direct Fits to $\sigma_{\rm los}(R)$

So far, we have made Bayesian inferences about MOND IFs based on Monte Carlo sampling of individual RARs and the stacked RAR. However, our MC sampling uses the likelihood function, which depends on the χ^2 of Equation (1). Therefore, it is interesting to ask whether the RAR step is necessary: is simply fitting to $\sigma_{\rm los}(R)$ sufficiently discriminating?

Figure 3 already shows the best-fitting cases for the ΛCDM models with a gNFW halo. Here, we consider similar checks within the MOND paradigm, for the Simple and McGaugh IFs with the fiducial value of a_0. To illustrate, of the 24 ATLAS^{3D} galaxies, we only select galaxies having ellipticities $\varepsilon < 0.1$: they are NGC 4486, NGC 4636, NGC 5846, and NGC 6703, all of which are SRs (see Table 1 of Chae et al. 2019 and references therein).

As shown in Figure 16, for NGC 5846 and NGC 6703 (bottom two sets of panels), both the IFs reproduce the observed velocity dispersion profiles reasonably well: $\bar{\chi}^2_{\rm min} \lesssim 2.5$. However, the McGaugh IF fails to provide a good fit to NGC 4636 (second from top, right); it has $\chi^2/N_{\rm dof} = 6.7$. At face value, this galaxy alone rules out the McGaugh IF as a viable MOND model. (Although we do not show it here, allowing a different a_0 does not improve χ^2 significantly.) For NGC 4486 (top), neither of the IFs provides an acceptable fit. (In contrast, Figure 3 shows that the gNFW does fit well.) Again, at face value, $\sigma_{\rm los}(R)$ of this one galaxy invalidates both the Simple and McGaugh functions as viable MOND IFs. Considering the significance of this result, it is important to investigate more spherical galaxies selected from large ongoing and future IFS surveys such as MaNGA (see Section 6).

5. Systematic Errors?

When inferring the ratio $a_{\rm X}/a_{\rm B}$ in the supercritical acceleration regime, we marginalized over the $M_\star/L$ amplitude $\Upsilon_{\star 0}$, the gradient strength parameter K in Equation (10), and the DM/PM profile parameters. We have considered a reasonable range of functional forms for the IF or DM profile (Equations (4)–(6) and (12)) that leave little possibility of hidden systematic error associated with the chosen functional forms of the IF or DM profile. However, is it possible that our treatment of the $M_\star/L$ gradient, Equation (10) with $A = 2.33$ and $B = 6$, is too restrictive? Whereas the ratio A/B determines the radius within which the gradient matters, the product KA determines $(M_\star/L)_{R=0}/(M_\star/L)_{\rm outer}$, Given that we already consider $0 \leqslant K < 1.5$, there is no need to consider varying A as well. Therefore, we have studied how our results change if we change B (recall that $A/B = 0.4$ is indicated by current data).

Setting $B = 3$ or 9 ($R_{\rm lim} \approx 0.8R_{\rm e}$ or $0.25R_{\rm e}$; recall that current data prefer $R_{\rm lim} \approx 0.4R_{\rm e}$) makes little difference to the inferred ratio $a_{\rm X}/a_{\rm B}$, although the posterior PDFs of K are shifted. (The limiting cases of $B \to 0$ or ∞ would be equivalent to the case without a gradient.) Figure 17 shows

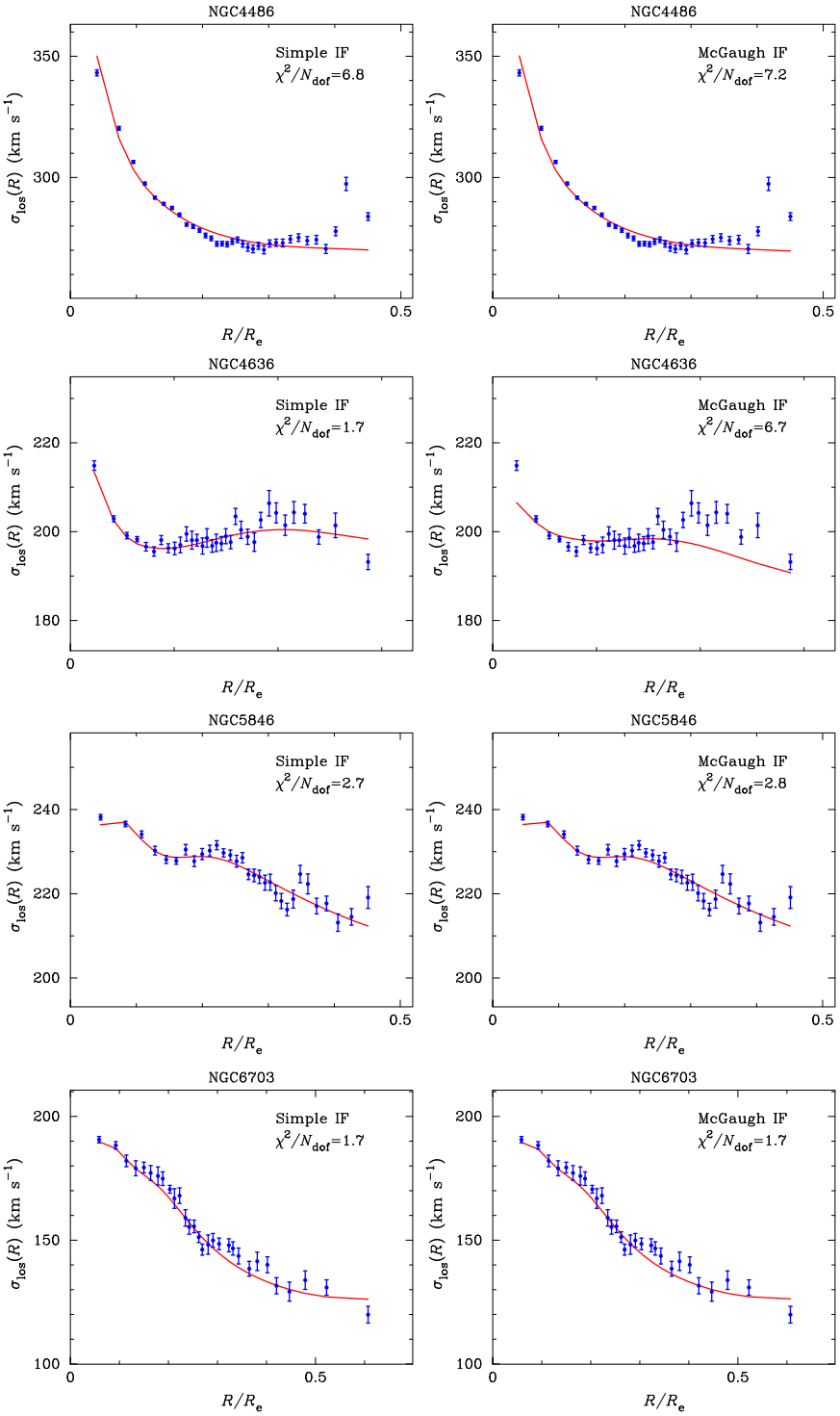

Figure 16. Observed and best-fit $\sigma_{\rm los}(R)$ profiles associated with the Simple and McGaugh IFs with $a_0 = 1.2 \times 10^{-10}$ m s^{-2}, for four "spherical" galaxies (ellipticities $\varepsilon < 0.1$).

results with $B = 3$. Thus, our results on $a_{\rm X}/a_{\rm B}$ are robust with respect to the choice of the gradient model unless it is dramatically different from Equation (10).

Could our finding that the Simple IF (Equation (4) with $\nu = 1$) is preferred still be systematically in error? Our numerical experiments show that McGaugh's IF could be preferred if we assume *no* $M_\star/L$ gradient ($K = 0$) in any galaxies *and* the MOND IF given by Equation (5) (or the Einasto 1965 DM profile) is assumed. On the other hand, if all elliptical galaxies have very strong $M_\star/L$ gradients ($K \gtrsim 1.2$), then Bekenstein's IF would be preferred. However, as we discuss below, we believe these extreme cases are unlikely.

As we discuss in the Introduction, the total lack of any gradient ($K = 0$) for all elliptical galaxies is not supported by a host of current observational studies. Our own Bayesian inferences (Chae et al. 2018) also do not support the absence

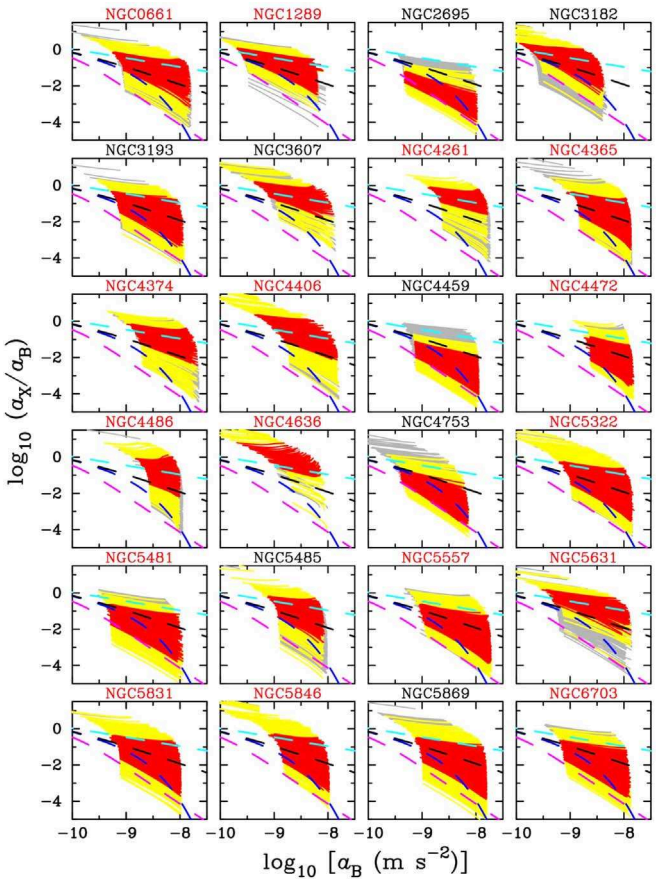

Figure 17. Results with an artificially chosen value of $B = 3$ in Equation (10) that allows a smoother radial gradient over a radial range up to $0.8R_e$, larger than the van Dokkum et al. (2017) limit of $0.4R_e$. The results on the ratio a_X/a_B are little changed compared with those shown in Figure 6.

of gradient, although there are some cases where a weak gradient appears likely. Very strong gradients ($K \gtrsim 1.2$) for *all* elliptical galaxies are also unlikely; $K = 1$ is already on the highest side of the spectrum of current observational results.

6. Discussion

We have obtained an empirical RAR $a_X/a_B \approx 10^{-1}\, a_{+1}/a_B$ around $a_{+1} \equiv 10^{+1}\, a_0$ in the supercritical acceleration regime $a_0 < a_B < 10^2 a_0$ through Bayesian inferences based on a host of MC sets of nearly spherical galaxies. This estimate, as unbiased a result as possible, can narrow down DM/PM phenomenologies in galactic astrophysics—and hence, theoretical models of DM and modified dynamics or gravity as well. Verlinde's emergent gravity, Bekenstein's IF, and the McGaugh et al. proposal of the exponentially decaying RAR (the Planck-like function) in the supercritical regime up to $100a_0$ are all inconsistent at $>4\sigma$ with our results. For example, for McGaugh's function to be valid in the supercritical acceleration regime, we must assume constant $M_\star/L$ in the central regions of *all* elliptical galaxies with the exponential IF (Equation (5)) (or the Einasto 1965 DM profile). At the other extreme, for Bekenstein's theory and Verlinde's theory to be valid in the supercritical acceleration regime, we must assume *all* ellipticals have stronger $M_\star/L$ gradients than the strongest reported to date.

A direct χ^2 test of the McGaugh IF using the spherical galaxy NGC 4636 also rules it out, as shown in Figure 16. Our results clearly support an RAR that can be described by the Simple IF as a mean (stacked) property. This result may well contain important information about DM properties or the property of gravity. Interestingly, the recently proposed scenario of baryon–DM interactions by Famaey et al. (2018) is fully consistent with our empirical RAR.

In this context, it is worth noting that our present study is not a rigorous test of whether a universal RAR exists in elliptical galaxies, nor whether a universal acceleration scale a_0 exists, although we have investigated individual PDFs of MOND IF profiles (see Section 4.4). Nor do we have a particular paradigm in mind. Rather, we have tried to extract the most information on DM or MG from the data. The ongoing debate on the issue of the presence/absence of a universal RAR in rotating galaxies (Kroupa et al. 2018; McGaugh et al. 2018; Rodrigues et al. 2018) is also relevant for dispersion-dominated elliptical galaxies. If a universal RAR truly exists, then both rotating and nonrotating galaxies must imply the same relation.

Our empirical RAR in the supercritical regime is not matched by the MUGS simulations of galaxy formation and evolution within the ΛCDM paradigm (Figure 9). Because the other inputs to our ΛCDM estimate of the RAR (stellar-to-halo mass ratios, halo profiles, and concentrations) are standard, the disagreement suggests that our empirical RAR provides a useful constraint on galaxy formation models within the context of ΛCDM.

While our present exploratory analysis of the supercritical acceleration regime of elliptical galaxies demonstrates the potential of using elliptical galaxies in addressing the DM problem, it also highlights the importance of quantifying $M_\star/L$ gradients. Large IFS samples, such as those provided by the MaNGA survey (Bundy et al. 2015), will allow a better determination of both $\sigma_{los}(R)$ and $M_\star/L$ gradients. Therefore, we hope our exploratory analysis motivates a more precise determination of the RAR in these larger samples.

We thank J. Khoury and M. van Putten for interesting and stimulating discussions. We also thank them and M. Trodden for comments on the draft. We are grateful to M. Cappellari for useful communications regarding the ATLAS^{3D} results. We also would like to thank A. Kosowsky for constructive criticisms, and an anonymous referee for insightful comments that helped us improve the analysis, presentation, and discussion. This work was initiated at the University of Pennsylvania while KHC was on sabbatical leave in 2017. This research was supported by the Basic Science Research Program through the National Research Foundation of Korea (NRF), funded by the Ministry of Education (NRF-2016R1D1A1B03935804). M.B. acknowledges NSF AST/1816330 for support.

Appendix A
Comments on Monte Carlo Sampling: SMC versus MCMC

All the results in the main text use sets of parameters generated through MC sampling algorithms. We have considered two algorithms: the SMC (our own algorithm written

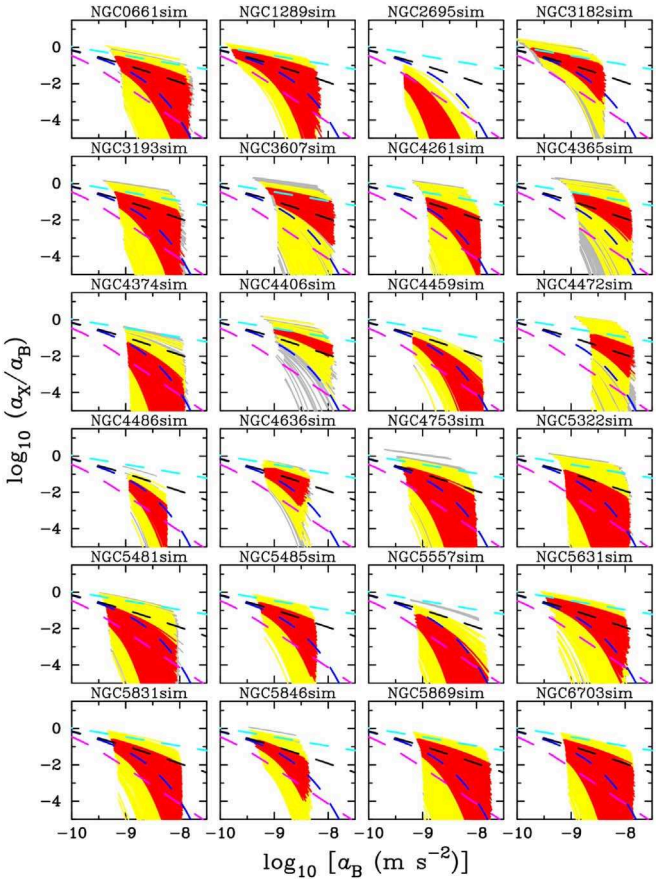

Figure 18. Same as Figure 10, but through the MCMC sampler.

by K.-H. C.) and the MCMC implemented in the "emcee" package (Foreman-Mackey et al. 2013). The SMC produces MC models that satisfy a certain criterion ($\bar{\chi}^2 < \bar{\chi}^2_{\rm crit}$), without any correlation between successive iterations. Consequently, this method is slow, but it searches the entire parameter space within the prior ranges. Theoretically, it is based on a top-hat likelihood function, but the resulting posterior PDF of a parameter is not a top-hat shape, because the PDF of $\bar{\chi}^2$ in the accepted parameter space does not follow a top-hat shape. Although this method is rather crude, tests using mock velocity dispersion profiles (see Section 4.1) indicate that it is robust and reasonably satisfies the expected statistics (albeit conservatively rather than accurately).

The MCMC method produces correlated MC models through self-proposed covariance matrices between iterations after a sufficient number of initial iterations. The algorithm is efficient and sophisticated—and hence, popular. We have tested it with a Gaussian likelihood (Equation (15)), using the same mock velocity dispersion profiles as in Section 4.1. Figure 18 shows the analog of Figure 10. Compared with the SMC, the MCMC returns narrower distributions of $a_{\rm X}/a_{\rm B}$. However, in some cases, the posterior distributions actually rule out the input model (in this case, the McGaugh IF)! This is particularly so for NGC2695sim. This indicates that emcee with the Gaussian likelihood can sometimes return unrealistically narrow (overconfident) results. This difficulty did not arise with the SMC, which is why we showed both SMC and MCMC sampling results in the main text.

Appendix B
Correlation of Parameters from the MCMC Sampling in the ΛCDM Case

We provide examples of the correlation of parameters from the MCMC sampling of models in the ΛCDM case. For this purpose, we chose the four roundest galaxies that can be modeled most reliably using spherical models: NGC 4486, 4636, 5846, and 6703. Figure 19 exhibits the results.

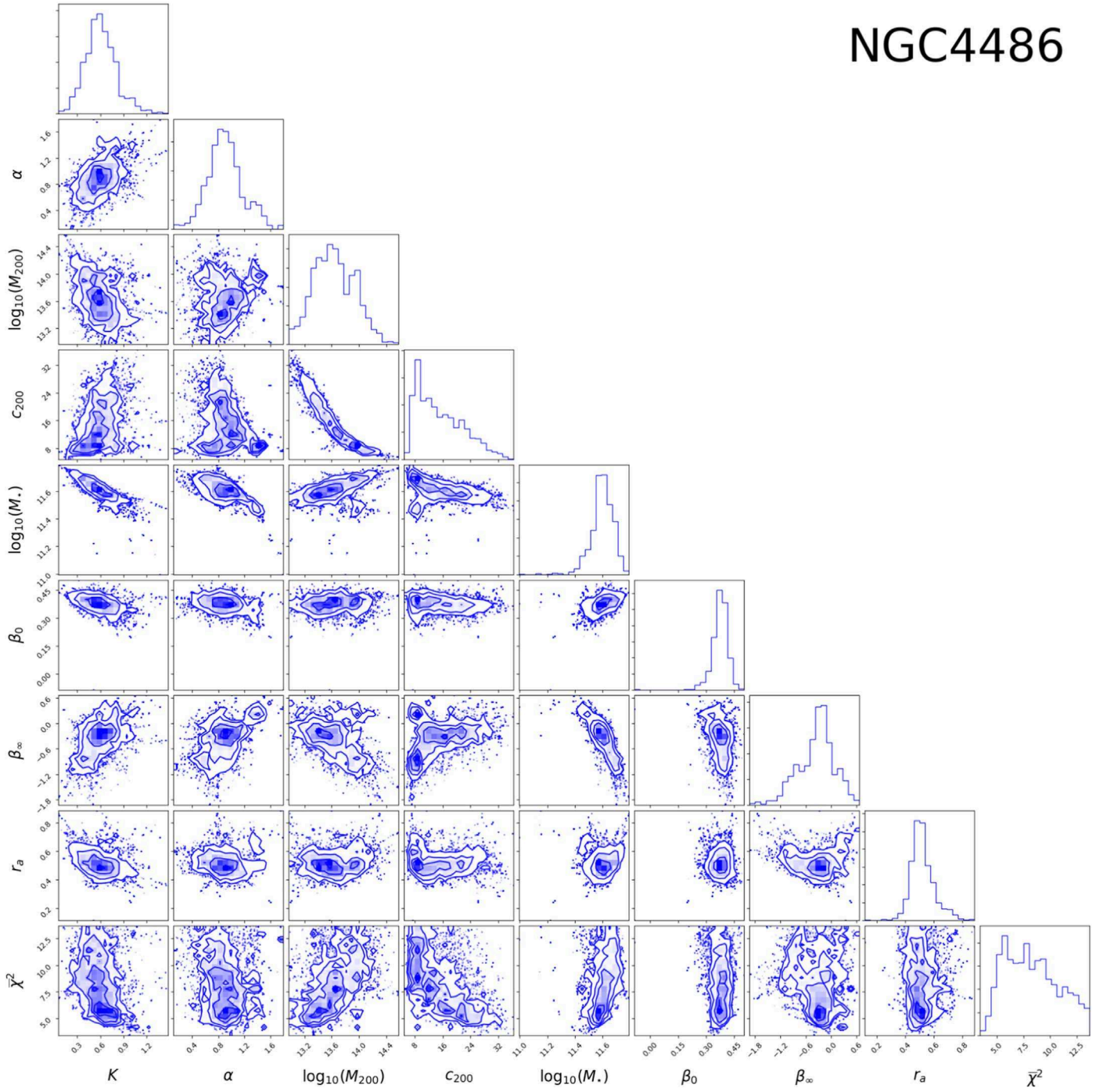

Figure 19. Correlation of parameters (Table 2) in the ΛCDM case through the MCMC sampler. Here, stellar mass $M_\star$ refers to $\Upsilon_{\star 0} \times L_{r,\mathrm{MGE}}$, where $L_{r,\mathrm{MGE}}$ is the luminosity of the MGE light distribution in the SDSS r-band.

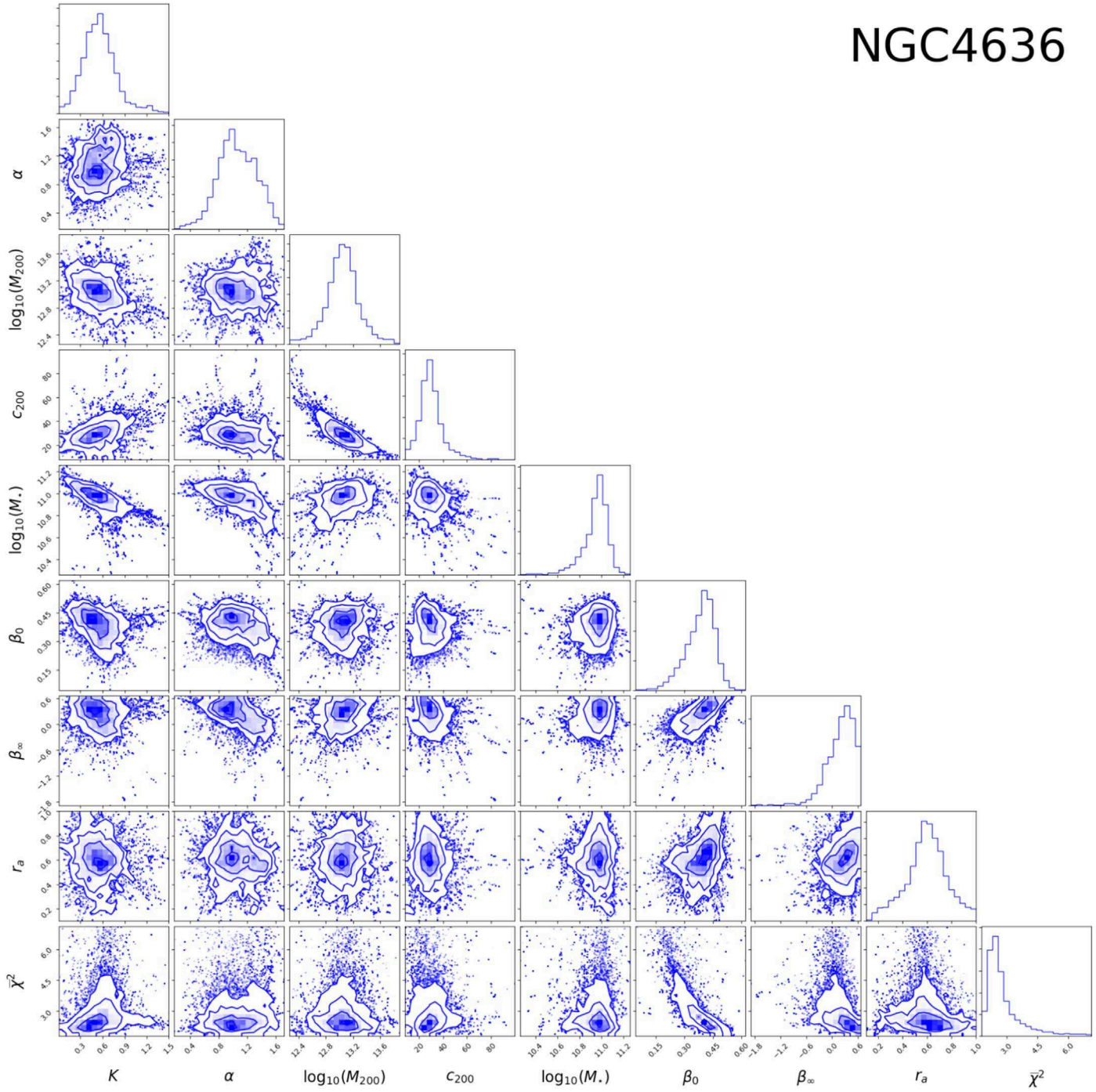

Figure 19. (Continued.)

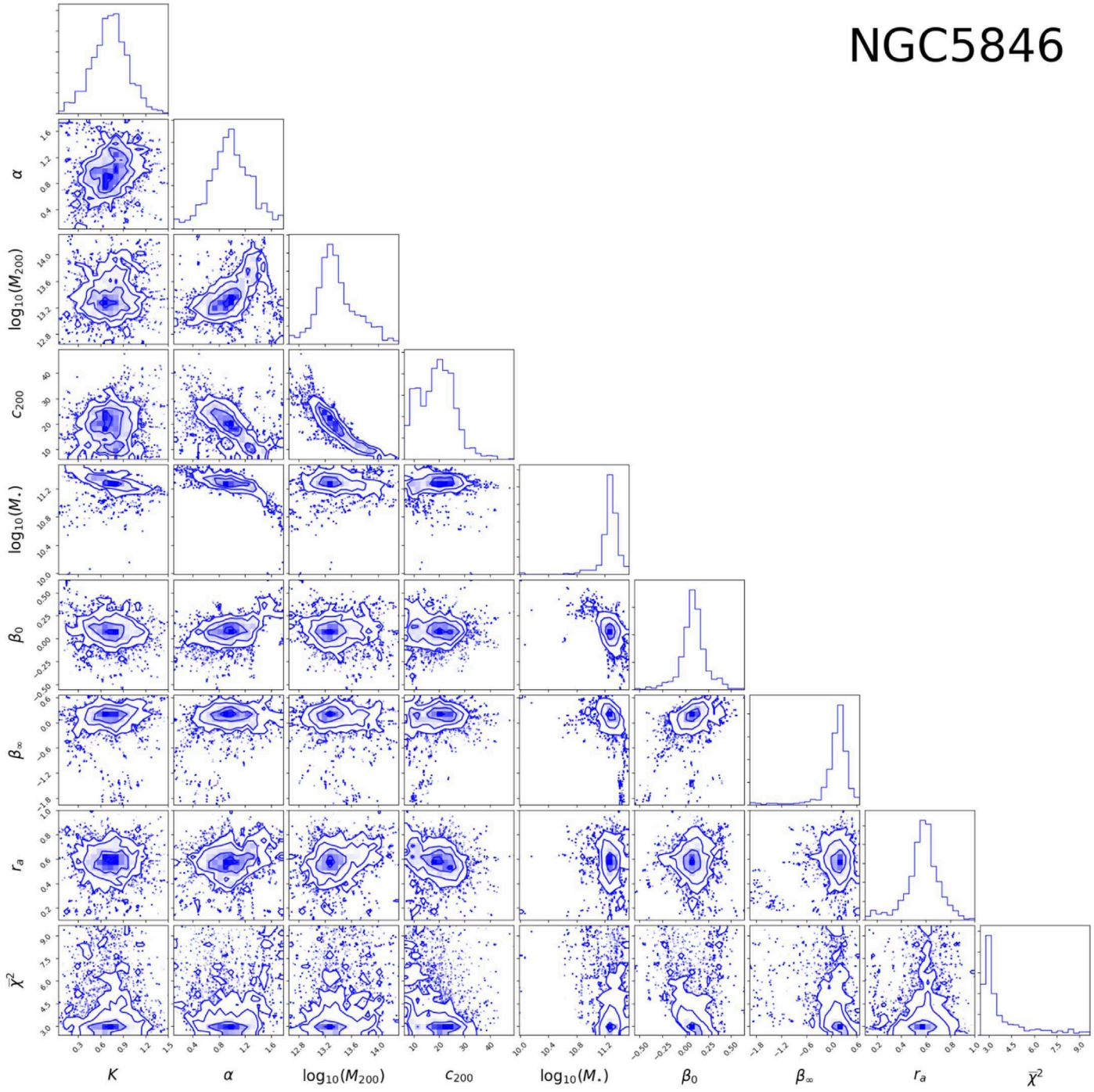

Figure 19. (Continued.)

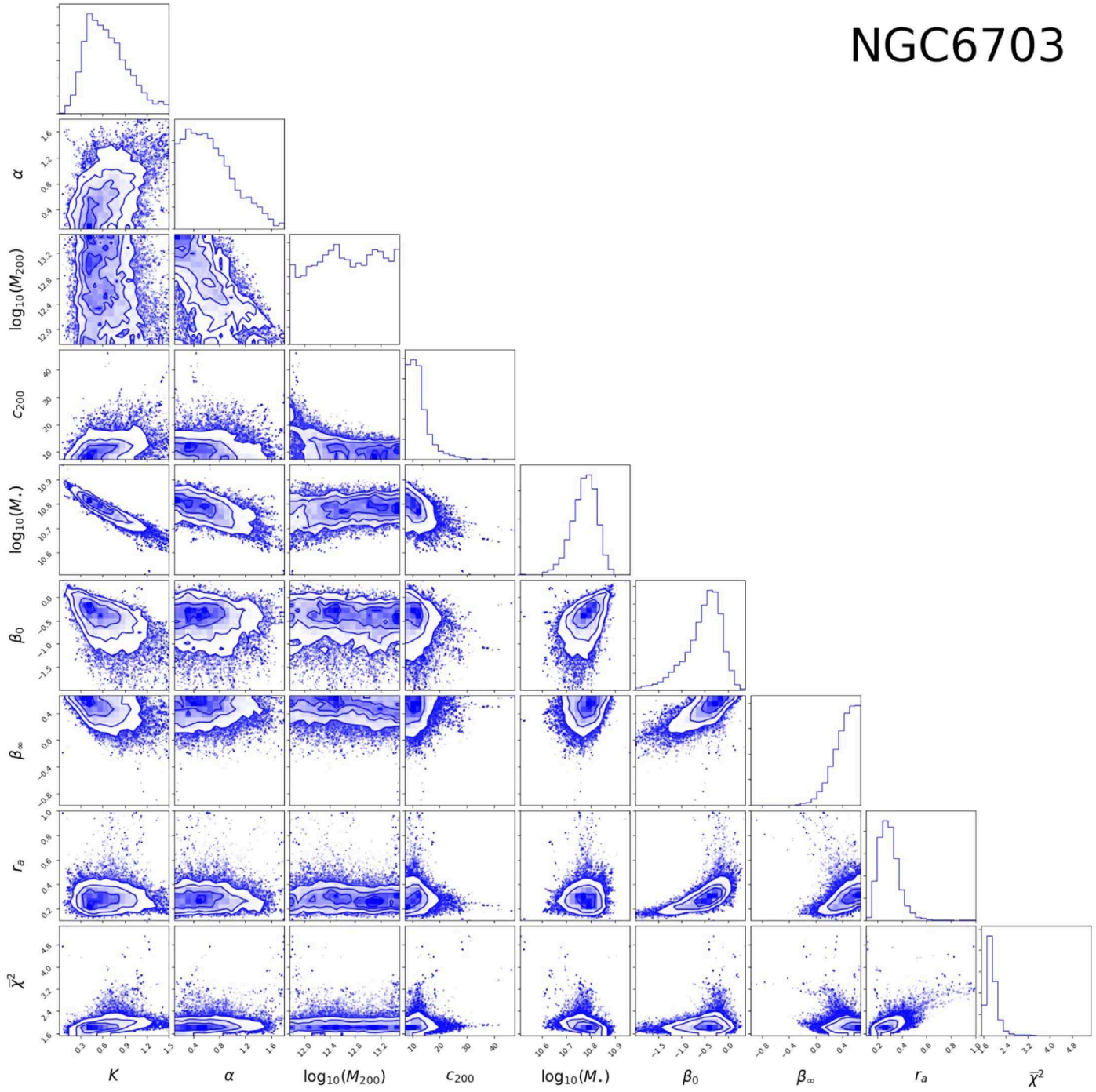

Figure 19. (Continued.)

ORCID iDs

Kyu-Hyun Chae https://orcid.org/0000-0002-6016-2736
Ravi K. Sheth https://orcid.org/0000-0002-2330-0917

References

Abazajian, K. N., Adelman-McCarthy, J. K., Agüeros, M. A., et al. 2009, ApJS, 182, 543
Allison, R., & Dunkley, J. 2014, MNRAS, 437, 3918
Alton, P. D., Smith, R. J., & Lucey, J. R. 2017, MNRAS, 468, 1594
Alton, P. D., Smith, R. J., & Lucey, J. R. 2018, MNRAS, 478, 4464
Bekenstein, J. D. 2004, PhRvD, 70, 083509
Berezhiani, L., & Khoury, J. 2015, PhRvD, 92, 103510
Bernardi, M., Sheth, R. K., Dominguez-Sanchez, H., et al. 2018, MNRAS, 477, 2560
Bertone, G., & Tait, T. M. P. 2018, Natur, 562, 51
Binney, J., & Tremaine, S. 2008, Galactic Dynamics (2nd ed.; Princeton, NJ: Princeton Univ. Press)
Blanchet, L., & Le Tiec, A. 2009, PhRvD, 80, 023524
Bundy, K., Bershady, M. A., Law, D. R., et al. 2015, ApJ, 798, 7
Burrage, C., Copeland, E. J., & Millington, P. 2017, PhRvD, 95, 064050
Cappellari, M., Emsellem, E., Krajnović, D., et al. 2011, MNRAS, 413, 813
Chae, K.-H., Bernardi, M., & Kravtsov, A. V. 2014, MNRAS, 437, 3670
Chae, K.-H., Bernardi, M., & Sheth, R. K. 2018, ApJ, 860, 81
Chae, K.-H., Bernardi, M., & Sheth, R. K. 2019, ApJ, 874, 41
Chae, K.-H., & Gong, I.-T. 2015, MNRAS, 451, 1719
Davis, T. A., & McDermid, R. M. 2017, MNRAS, 464, 453
Desmond, H. 2017, MNRAS, 464, 4160

Diemer, B., & Kravtsov, A. V. 2015, ApJ, 799, 108
Einasto, J. 1965, TrAlm, 5, 87
Famaey, B., & Binney, J. 2005, MNRAS, 363, 603
Famaey, B., Khoury, J., & Penco, R. 2018, JCAP, 03, 038
Famaey, B., & McGaugh, S. S. 2012, LRR, 15, 10
Foreman-Mackey, D., Hogg, D. W., Lang, D., & Goodman, J. 2013, PASP, 125, 306
Gerhard, O., Kronawitter, A., Saglia, R. P., & Bender, R. 2001, AJ, 121, 1936
Janz, J., Cappellari, M., Romanowsky, A. J., et al. 2016, MNRAS, 461, 2367
Keller, B. W., & Wadsley, J. W. 2017, ApJL, 835, 17
Kent, S. M. 1987, AJ, 93, 816
Kroupa, P. 2002, Sci, 295, 82
Kroupa, P., Banik, I., Haghi, H., et al. 2018, NatAs, 2, 925
La Barbera, F., Vazdekis, A., Ferreras, I., et al. 2016, MNRAS, 457, 1468
Lelli, F., McGaugh, S. S., Schombert, J. M., & Pawlowski, M. S. 2017, ApJ, 836, 152
Li, P., Lelli, F., McGaugh, S., & Schombert, J. 2018, A&A, 615, 70
Ludlow, A. D., Benitez-Llambay, A., Schaller, M., et al. 2017, PhRvL, 118, 1103
Mandelbaum, R., Seljak, U., & Hirata, C. M. 2008, JCAP, 08, 006
Mandelbaum, R., Wang, W., Zu, Y., et al. 2016, MNRAS, 457, 3200
Martín-Navarro, I., La Barbera, F., Vazdekis, A., Falcón-Barroso, J., & Ferreras, I. 2015, MNRAS, 447, 1033
McGaugh, S. 2008, ApJ, 683, 137
McGaugh, S. S. 2004, ApJ, 609, 652
McGaugh, S. S., Lelli, F., & Schombert, J. M. 2016, PhRvL, 117, 201101
McGaugh, S. S., Li, P., Lelli, F., & Schombert, J. M. 2018, NatAs, 2, 924
Meert, A., Vikram, V., & Bernardi, M. 2015, MNRAS, 446, 3943
Milgrom, M. 1983, ApJ, 270, 371
Milgrom, M. 2012, PhRvL, 109, 131101
Navarro, J. F., Benítez-Llambay, A., Fattahi, A., et al. 2017, MNRAS, 471, 1841
Navarro, J. F., Frenk, C. S., & White, S. D. M. 1997, ApJ, 490, 493
Oldham, L., & Auger, M. 2018, MNRAS, 474, 4169
Rodrigues, D. C., Marra, V., del Popolo, A., & Davari, Z. 2018, NatAs, 2, 668
Sanders, R. H., & Noordermeer, E. 2007, MNRAS, 379, 702
Sarzi, M., Spiniello, C., La Barbera, F., Krajnović, D., & van den Bosch, R. 2018, MNRAS, 478, 4084
Shankar, F., Sonnenfeld, A., & Mamon, G. A. 2017, ApJ, 840, 34
Sonnenfeld, A., Leauthaud, A., Auger, M. W., et al. 2018, MNRAS, 481, 164
Sonnenfeld, A., Treu, T., Marshall, P. J., et al. 2015, ApJ, 800, 94
Tenneti, A., Mao, Y.-Y., Croft, R. A. C., et al. 2018, MNRAS, 474, 3125
van Dokkum, P., Conroy, C., Villaume, A., Brodie, J., & Romanowsky, A. J. 2017, ApJ, 841, 68
van Putten, M. H. P. M. 2018, MNRAS, 481L, 26
Verlinde, E. P. 2017, ScPP, 2, 016
Wall, J. V., & Jenkins, C. R. 2012, Practical Statistics for Astronomers (2nd ed.; Cambridge: Cambridge Univ. Press)